SPAWAR

**Systems Center
PACIFIC**

A Near-to-Far Field Transformation
Using Spherical Expansions
Phase 1: Verification on Simulated Antennas

J. H. Meloling
J. C. Allen

SSC Pacific
San Diego, CA 92152-5001

SB

Executive Summary

High-Frequency (HF) antenna design is challenged by advanced HF communication systems, such as HF-MIMO and HF-NVIS for vehicular units, and the new vector-sensing HF direction-finding systems. These systems require small, wideband, and efficient HF antennas with specified radiation patterns. Regardless of the tradeoffs that are made to get to a specific HF antenna, its far-field pattern is the final governance of system performance.

Measuring far-field HF patterns is challenging—HF wavelengths range from 10 m at 30 MHz to 100 m at 3 MHz. Typical pattern ranges measure the electric field on a hemisphere with a radius 10 wavelengths from the antenna. Consequently, an HF pattern range requires a 1-km radius and necessitates other approaches. One approach measures the near field on a standard pattern range and extends the resulting near-field model to a far-field estimate.

Tapan Sarkar wrote a substantial technical paper on "near-to-far" transformation using spherical expansions [12]. An implementation of Sarkar's near-to-far transformation is assessed in this report. Phase 1 of this report assesses this implementation on the following antenna models:

- Analytic antenna models where the near field, far field, and the spherical expansions are computable in closed form.

- Mini-NEC antenna simulations where the near and far fields are computable and numerical quadratures obtain the spherical expansions.

This implementation does recover the far field from the near field—provided the spherical expansion includes a sufficient number of terms. Phase 2 applies this expansion to pattern-range measurements and extends the implementation to estimate the number of terms and account for measurement noise.

Contents

List of Figures

List of Tables

1 HF Antenna Measurements

HF antenna design is challenged by advanced HF communication systems and developments in HF direction finding. Figure 1 shows a recent HF-NVIS antenna developed for ground-mobile applications. Challenges for any compact HF-NVIS antenna are the trade-offs between bandwidth, pattern (upward radiation), and efficiency with the necessary adaptive tuning. This antenna and its inevitable tradeoffs should be verified by measurements.

Figure 1: Compact HF-NVIS antenna for vehicle and ground forces (Reproduced by permission of Military Hi-Q [9]).

Figure 2 shows co-located HF antennas for direction finding. Rather than an HF array with the half-wavelength spacing, this co-located array offers direction finding using polarization rather than spatial diversity. One challenge for HF vector sensors is array calibration. Array calibration for a co-located HF array is equivalent to measuring the array's response to an electric field for each azimuth, elevation, and polarization.

Figure 2: Compact HF direction-finding antenna (Reproduced by permission of the Institution of Engineering & Technology [11]).

Consequently, both the HF-NVIS antennas and HF vector sensors require far-field measurements to establish antenna performance. Figure 3 shows the Antenna Pattern Range located at the Model Range, Space and Naval Warefare Systems Center Pacific (SSC Pacific). The electric field produced by an antenna placed in the Antenna Pattern Range is measured over the upper hemisphere at a radius of approximately 80 ft (24 m). For 3-MHz HF antennas, the Antenna Pattern Range measures their near fields at 24 m or 1/4 wavelength. For 30-MHz HF antennas, their near fields are measured at 2.4 wavelengths. This variation in the near-field measurements raises the following question: *Is the near-to-far transform stable with respect to Antenna Pattern Range measurements ranging over 0.25 to 2.4 wavelengths?*

Figure 3: Antenna Pattern Range at SSC Pacific.

This report assesses a near-to-far transformation with the goal of mapping the near-field measurements taken on a grid of azimuth and elevation angles on the Antenna Pattern Range into far-field patterns. Because the far-field pattern is not directly measurable, this Phase 1 discussion relies on bounding the error in analytic models before undertaking the leap to the Antenna Pattern Range measurements. Accordingly, Section 2 reviews the near-to-far transformation and its discrete implementation with the errors arising from truncation of the spherical sums and the discrete sampling of the electric field.

Section 3 reviews Tapan Sarkar's near-to-far transformation [12]. The spherical expansions and the special functions are made explicit with correct normalizations, end points of the expansions, and three-term recurrence relations are supported for computational processing.

Sections 4–11 apply the near-to-far transform to selected antenna models. Each section undertakes the near-field and far-field models of an antenna, an "analysis" of the near field in spherical modes using only discrete samples of the electric field, and a comparison the resulting synthetic spherical expansion against the modeled antenna in both the near and far fields. These examples show that controlling the truncation error is more critical than the discretization errors. That is, sampling the electric field at 5° to 18° increments (discretization error) contributes less error than omitting higher-order terms in the spherical expansion (truncation error).

The final section outlines the tasking for Phase 2 where the near-to-far transformation will be applied to measurements collected on the Antenna Pattern Range.

2   Near-to-Far Field Transformations

A canonical problem in antenna engineering is estimating the inaccessible far field from near-field measurements. This report assesses one implementation of Tapan Sarkar's "near-to-far" transformation [12]. Figure 4 illustrates this near-to-far implementation.
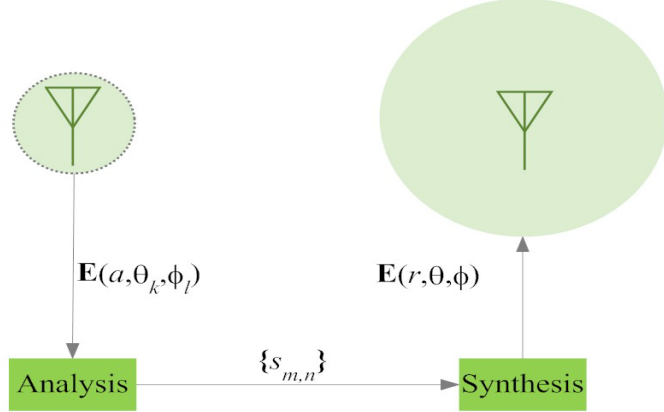
Figure 4: Computational chart for the near-to-far transform.

Discrete near-field samples of the electric field are collected on a sphere of radius $r = a$. The "analysis" box uses these samples to compute electric-field coefficients $\{s_{m,n}\}$ by numerical quadratures. The main source of error in these coefficients $\{s_{m,n}\}$ arises from the discrete samples because the numerical quadratures operate on two-dimensional splines of the electric field samples. That is, the coefficients $\{s_{m,n}\}$ are accurate representations of an electric field recovered from the sampled electric field [6].

The "synthesis" box computes the electric field at any radius $r \geq a$ as a sum of Sarkar's orthonormal basis functions $\{\mathbf{e}_{m,n}\}$:

$$\mathbf{E}(r, \theta, \phi) = \sum_{n=0}^{\infty} \sum_{m=0}^{n} s_{m,n} \mathbf{e}_{m,n}(r, \theta, \phi) =: \mathfrak{S}(a; r, \theta, \phi). \tag{1}$$

The key observation is that the expansion holds regardless of the measurement sphere:

$$\mathfrak{S}(a_1; r, \theta, \phi) = \mathfrak{S}(a_2; r, \theta, \phi)$$

for $r \geq a_1, a_2$.

Assessing the quality of this expansion focuses not only on computing the far-field pattern using a truncated sum

$$\mathbf{E}(r, \theta, \phi) \approx \sum_{n=0}^{N} \sum_{m=0}^{n} s_{m,n} \mathbf{e}_{m,n}(r, \theta, \phi) =: \mathfrak{S}(a; N; r, \theta, \phi),$$

4

but a truncated sum where the coefficients of the expansion have accuracy limited by the discrete sampling:

$$
\begin{aligned}
\mathbf{E}(r, \theta, \phi) &\approx \sum_{n=0}^{N} \sum_{m=0}^{n} s_{m,n}(\Delta\theta, \Delta\phi) \mathbf{e}_{m,n}(r, \theta, \phi) \\
&=: \mathfrak{S}(a; \Delta\theta, \Delta\phi, N; r, \theta, \phi)
\end{aligned}
\tag{2}
$$

Thus, the expansion's accuracy is degraded by truncation error and limited by the discretization errors.

Phase 1 of this report assesses Sarkar's expansion on several antenna models. The Hertzian dipole is the baseline computational vehicle for Phase 1. The goal is to verify the numerical computation and the sensitivity of the approximation

$$
\mathbf{E}(r, \theta, \phi) \approx \mathfrak{S}(a; \Delta\theta, \Delta\phi, N; r, \theta, \phi)
$$

on this analytic dipole model. Once this ideal dipole is analyzed, other antennas models are treated in the same format: analysis, synthesis, and the far-field pattern. Figure 5 summarizes this process where the "ground truth" of the antenna model's electric field is compared against the synthetic field.
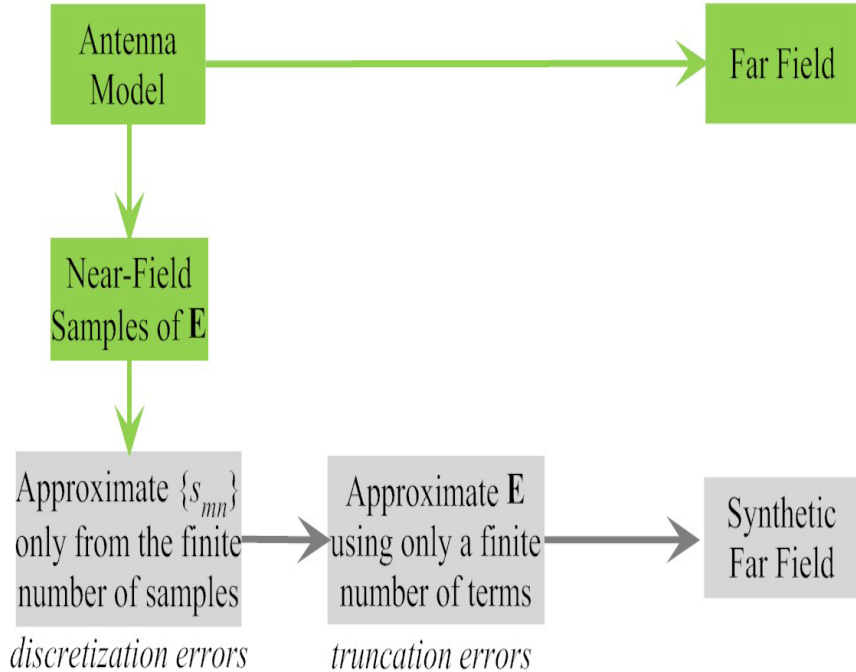
Figure 5: Flow chart of the near-to-far comparison using an antenna model.

Table 1: Notation.

Variable	Description
k	Wavenumber
λ	Wavelength (m)
f	Frequency (Hz)
ω	Frequency (rad/sec)
η	Free space impedance 120π (ohms)
ϵ	Permittivity (F/m)
r	Radius (m)
θ	Zenith (radians)
ϕ	Azimuth(radians)
$\mathbf{E}$	Electric field vector (V/m)
:=	Definition

3 Sarkar's Near-to-Far Transform

Figure 6 illustrates spherical coordinates and the decomposition of the electric field in the $\theta \times \phi$ plane. Sarkar expands the electric field using spherical Bessel functions of the second kind $h_n^{(2)}(kr)$, associated Legendre functions of the first kind $P_n^m(\cos(\theta))$ with argument $\cos(\theta)$, and coefficients α_{mn}, β_{mn}, γ_{mn}, and δ_{mn} determined by the near-field boundary [12, Equation 5]:

$$E_\theta(r, \theta, \phi) = j\omega\mu \sum_{n=0}^{\infty} \sum_{m=0}^{n} m h_n^{(2)}(kr) \frac{P_n^m(\cos(\theta))}{\sin(\theta)} \{\gamma_{mn} \sin(m\phi) - \delta_{mn} \cos(m\phi)\}$$

$$+ \sum_{n=0}^{\infty} \sum_{m=0}^{n} \frac{1}{r} \frac{\partial}{\partial r} \left(r h_n^{(2)}(kr) \right) \frac{dP_n^m(\cos(\theta))}{d\theta} \{\alpha_{mn} \cos(m\phi) + \beta_{mn} \sin(m\phi)\}.$$

and [12, Equation 6]

$$E_\phi(r, \theta, \phi) = j\omega\mu \sum_{n=0}^{\infty} \sum_{m=0}^{n} h_n^{(2)}(kr) \frac{dP_n^m(\cos(\theta))}{d\theta} \{\gamma_{mn} \cos(m\phi) + \delta_{mn} \sin(m\phi)\}$$

$$- \sum_{n=0}^{\infty} \sum_{m=0}^{n} \frac{1}{r} \frac{\partial}{\partial r} \left(r h_n^{(2)}(kr) \right) \frac{m P_n^m(\cos(\theta))}{\sin(\theta)} \{\alpha_{mn} \sin(m\phi) - \beta_{mn} \cos(m\phi)\}.$$
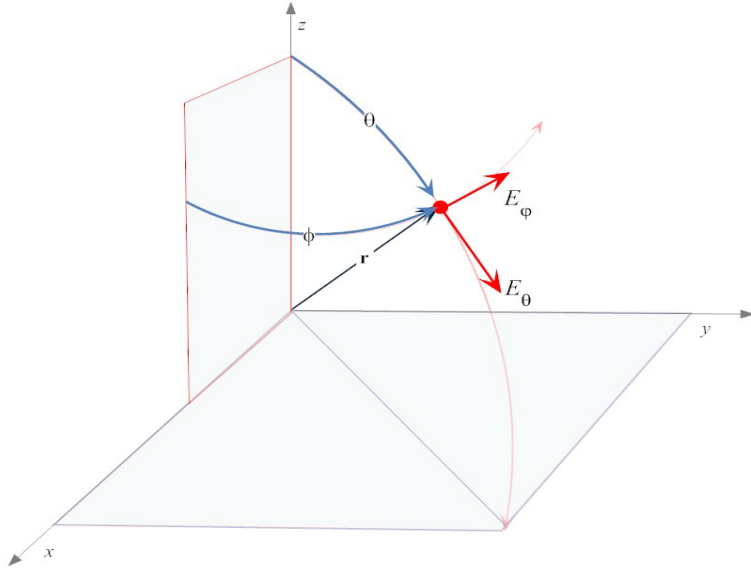
Figure 6: Spherical coordinates for the electric field showing the tangent vectors (E_r is omitted).

The coefficients are computed from the near field at radius $r = a$ [12, Equations 14 and 27]:

$$\alpha_{mn} = \frac{a}{kah_n^{(2)\prime}(ka) + h_n^{(2)}(ka)} \frac{(2n+1)(n-m)!}{2n(n+1)(n+m)!} \frac{\epsilon_m}{2\pi} \int_0^{2\pi} d\phi \int_0^{\pi} d\theta$$
$$\left\{ E_\theta(a,\theta,\phi) \frac{dP_n^m(\cos(\theta))}{d\theta} \sin(\theta)\cos(m\phi) - mE_\phi(a,\theta,\phi)P_n^m(\cos(\theta))\sin(m\phi) \right\},$$

[12, Equations 14 and Eq. 31]:

$$\beta_{mn} = \frac{a}{kah_n^{(2)\prime}(ka) + h_n^{(2)}(ka)} \frac{(2n+1)(n-m)!}{2n(n+1)(n+m)!} \frac{\epsilon_m}{2\pi} \int_0^{2\pi} d\phi \int_0^{\pi} d\theta$$
$$\left\{ E_\theta(a,\theta,\phi) \frac{dP_n^m(\cos(\theta))}{d\theta} \sin(\theta)\sin(m\phi) + mE_\phi(a,\theta,\phi)P_n^m(\cos(\theta))\cos(m\phi) \right\},$$

[12, Equations 13 and 32]:

$$\gamma_{mn} = \frac{1}{j\omega\mu h_n^{(2)}(ka)} \frac{(2n+1)(n-m)!}{2n(n+1)(n+m)!} \frac{\epsilon_m}{2\pi} \int_0^{2\pi} d\phi \int_0^{\pi} d\theta$$
$$\left\{ E_\phi(a,\theta,\phi) \frac{dP_n^m(\cos(\theta))}{d\theta} \sin(\theta)\cos(m\phi) + mE_\theta(a,\theta,\phi)P_n^m(\cos(\theta))\sin(m\phi) \right\},$$

[12, Equations 13 and 33]:

$$\delta_{mn} = \frac{1}{j\omega\mu h_n^{(2)}(ka)} \frac{(2n+1)(n-m)!}{2n(n+1)(n+m)!} \frac{\epsilon_m}{2\pi} \int_0^{2\pi} d\phi \int_0^{\pi} d\theta$$
$$\left\{ E_\phi(a,\theta,\phi) \frac{dP_n^m(\cos(\theta))}{d\theta} \sin(\theta)\sin(m\phi) - mE_\theta(a,\theta,\phi)P_n^m(\cos(\theta))\cos(m\phi) \right\}.$$

The twiddle factor is the standard adjustment for working with the sinusoidal basis:

$$\epsilon_m := \left\{ \begin{array}{ll} 1 & m = 0 \\ 2 & m > 0 \end{array} \right. .$$

The spherical Bessel functions of the second kind are defined in Arfken as [3, Equation 11.150]:

$$h_n^{(2)}(r) := \sqrt{\frac{\pi}{2r}} H_{n+1/2}^{(2)}(r), \tag{3}$$

where $H_n^{(2)}(r)$ is the Hankel function of the second kind. Figure 7 plots the first few

spherical Bessel functions [3, Equation 11.150]:

$$h_0^{(2)}(r) = \exp(-jr)\frac{j}{r}$$

$$h_1^{(2)}(r) = \exp(-jr)\left\{-\frac{1}{r} + \frac{j}{r^2}\right\}$$

$$h_2^{(2)}(r) = \exp(-jr)\left\{-\frac{j}{r} - \frac{3}{r^2} + \frac{j3}{r^3}\right\}.$$
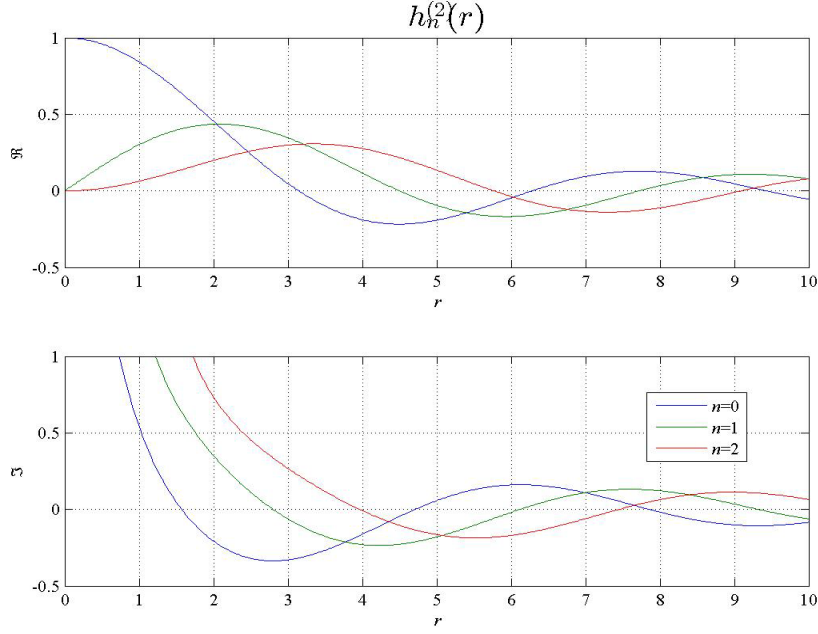
Figure 7: Spherical Bessel functions of the second kind.

The associated Legendre functions of the first kind $P_n^m(x)$ are [3, Equation 12.84 and footnote]:

$$P_n^m(x) := (-1)^m (1 - x^2)^{m/2}\frac{d^m}{dx^m}P_n(x),$$

where $P_n(x)$'s are the Legendre polynomials. There is the handy observation that

$$P_n^0(x) = P_n(x).$$

A stand-alone form adapted from [2, Equation 4.102]

$$P_n^m(x) := \frac{(-1)^m}{2^n n!}(1 - x^2)^{m/2}\frac{d^{m+n}}{dx^{m+n}}\left((x^2 - 1)^n\right) \tag{4}$$

9

that computes

$$P_n^m(x) = 0 \text{ for } m > n \tag{5}$$

Table 2 lists the initial Legendre polynomials and their derivatives. Figure 8 plots the first few Legendre polynomials.

Table 2: Legendre polynomials [3, Table 12.1].

n	$P_n(x)$	$P_n'(x)$
0	1	0
1	x	1
2	$\frac{1}{2}(3x^2 - 1)$	$3x$
3	$\frac{1}{2}(5x^3 - 3x)$	$\frac{1}{2}(15x^2 - 3)$
4	$\frac{1}{8}(35x^4 - 30x^2 + 3)$	$\frac{1}{2}(35x^3 - 15x)$
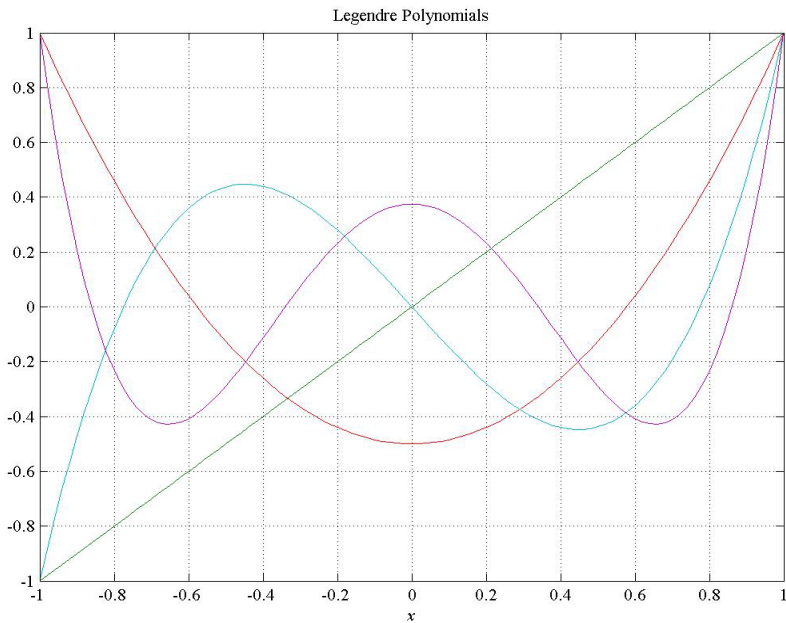
Figure 8: Legendre polynomials.

An ambiguity at $n = 0$ occurs because α_{mn}, β_{mn}, γ_{mn} and δ_{mn} contain a "1/0" term for $n = 0$. If these coefficients are finite, the contribution of $n = 0$ to the

near-to-far transformation is zero:

$$\sum_{n=0}^{0}\sum_{m=0}^{n} j\omega\mu m \frac{h_n^{(2)}(kr)}{\sin(\theta)} P_n^m(\cos(\theta))\{\gamma_{mn}\sin(m\phi) - \delta_{mn}\cos(m\phi)\}$$

$$+\sum_{n=0}^{0}\sum_{m=0}^{n} \frac{1}{r}\frac{\partial}{\partial r}\left(rh_n^{(2)}(kr)\right)\frac{dP_n^m(\cos(\theta))}{d\theta}\{\alpha_{mn}\cos(m\phi) + \beta_{mn}\sin(m\phi)\}$$

$$= \frac{1}{r}\frac{\partial}{\partial r}\left(rh_n^{(2)}(kr)\right)\frac{dP_0^0(\cos(\theta))}{d\theta}\alpha_{00}$$

$$= 0.$$

The last equality follows because the derivative of $P_0^0(x) = P_0(x) = 1$ is zero. Therefore, the near-to-far transformation starts the double sum at $n = 1$.

3.1 $dP_n^m(\cos(\theta))/d\theta$

Differentiating the generating function [3, Equation 12.84] computes this derivative in terms of these functions. Recall that $P_n^0(x) = P_n(x)$ denotes the Legendre polynomials. If $0 \le m < n$,

$$\frac{dP_n^m(x)}{dx} = \frac{d}{dx}\left\{(-1)^m(1-x^2)^{m/2}\frac{d^m}{dx^m}P_n(x)\right\}$$

$$= -(-1)^m m(1-x^2)^{m/2-1}x\frac{d^m}{dx^m}P_n(x) + (-1)^m(1-x^2)^{m/2}\frac{d^{m+1}}{dx^{m+1}}P_n(x)$$

$$= -m\frac{x}{1-x^2}(-1)^m(1-x^2)^{m/2}\frac{d^m}{dx^m}P_n(x)$$

$$\quad -(-1)^{m+1}(1-x^2)^{-1/2}(1-x^2)^{(m+1)/2}\frac{d^{m+1}}{dx^{m+1}}P_n(x)$$

$$= -m\frac{x}{1-x^2}P_n^m(x) - (1-x^2)^{-1/2}P_n^{m+1}(x).$$

In terms of the elevation angle,

$$\frac{dP_n^m(\cos(\theta))}{d\theta} = \frac{dP_n^m(x)}{dx}\frac{dx}{d\theta}$$

$$= \left\{-m\frac{x}{1-x^2}P_n^m(x) - (1-x^2)^{-1/2}P_n^{m+1}(x)\right\}(-\sin(\theta))$$

$$= \left\{m\frac{\cos(\theta)}{\sin^2(\theta)}P_n^m(\cos(\theta)) + \frac{1}{\sin(\theta)}P_n^{m+1}(\cos(\theta))\right\}\sin(\theta)$$

$$= m\cot(\theta)P_n^m(\cos(\theta)) + P_n^{m+1}(\cos(\theta)).$$

11

If $m = n$, the $(n+1)$ derivative of $P_n(x)$ is zero using $P_n^{n+1}(x) = 0$ from Equation 4. Consequently,

$$\frac{dP_n^m(\cos(\theta))}{d\theta} = m\cot(\theta)P_n^m(\cos(\theta)) + P_n^{m+1}(\cos(\theta)) \tag{6}$$

holds for all $0 \le m \le n$. When this derivative is weighted by the sine function,

$$\frac{dP_n^m(\cos(\theta))}{d\theta}\sin(\theta) = m\cos(\theta)P_n^m(\cos(\theta)) + \sin(\theta)P_n^{m+1}(\cos(\theta)), \tag{7}$$

3.2 $\partial/\partial r\left(rh_n^{(2)}(kr)\right)$

The radial term is computed from the spherical Hankel function of the second kind using the three-term recurrence relation [1, Equation 10.1.12]:

$$h_n^{(2)\prime}(r) = h_{n-1}^{(2)}(r) - \frac{n+1}{r}h_n^{(2)}(r).$$

Consequently, the derivative of the spherical Hankel functions can be computed using these functions themselves:

$$\begin{aligned}
\frac{\partial}{\partial r}\left(rh_n^{(2)}(kr)\right) &= h_n^{(2)}(kr) + krh_n^{(2)\prime}(kr) \\
&= h_n^{(2)}(kr) + kr\left\{h_{n-1}^{(2)}(kr) - \frac{n+1}{kr}h_n^{(2)}(kr)\right\} \\
&= krh_{n-1}^{(2)}(kr) - nh_n^{(2)}(kr). \tag{8}
\end{aligned}$$

The interpretation of [12, Equation 14] is computed as follows:

$$N = \frac{\partial}{\partial r}\left(rh_n^{(2)}(kr)\right)\Big|_{r=a} = kah_{n-1}^{(2)}(ka) - nh_n^{(2)}(ka).$$

4   Hertzian Electric Dipole

The Hertzian dipole is the baseline to assess Sarkar's spherical expansion. Figure 9 illustrates spherical coordinates around a short antenna carrying a $\widehat{\mathbf{z}}$-directed current i_A in free space on a wire of length $\Delta\ell$.
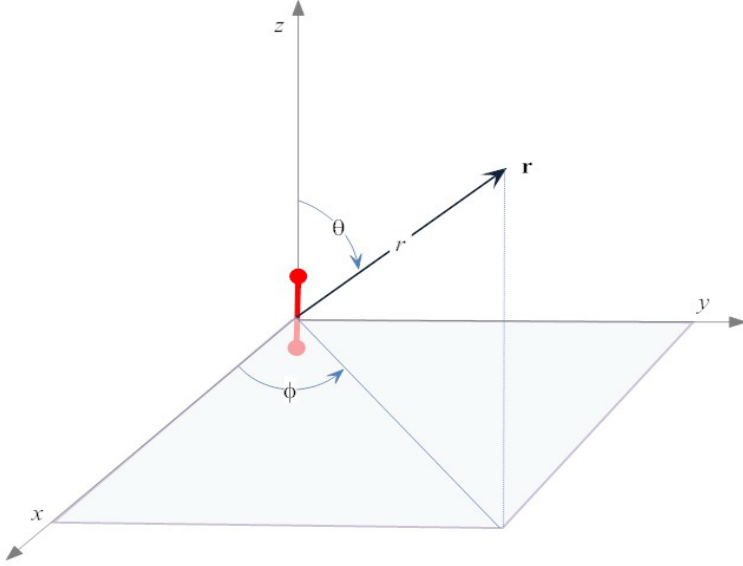
Figure 9: Hertzian dipole in spherical coordinates: $\mathbf{r} = r\widehat{\mathbf{r}}(\theta, \phi)$.

The next two figures present the nonzero magnetic and electric fields of the Hertzian dipole [7, Section 17.2]:

$$
\begin{aligned}
H_\phi(r,\theta,\phi) &= \frac{i_A\Delta\ell}{4\pi}k^2\sin(\theta)\exp(-jkr)\left\{\frac{j}{kr} + \frac{1}{(kr)^2}\right\}, \\
E_r(r,\theta,\phi) &= \eta\frac{i_A\Delta\ell}{2\pi}k^2\cos(\theta)\exp(-jkr)\left\{\frac{1}{(kr)^2} - \frac{j}{(kr)^3}\right\}, \\
E_\theta(r,\theta,\phi) &= \eta\frac{i_A\Delta\ell}{4\pi}k^2\sin(\theta)\exp(-jkr)\left\{\frac{j}{kr} + \frac{1}{(kr)^2} - \frac{j}{(kr)^3}\right\}.
\end{aligned}
\tag{9}
$$
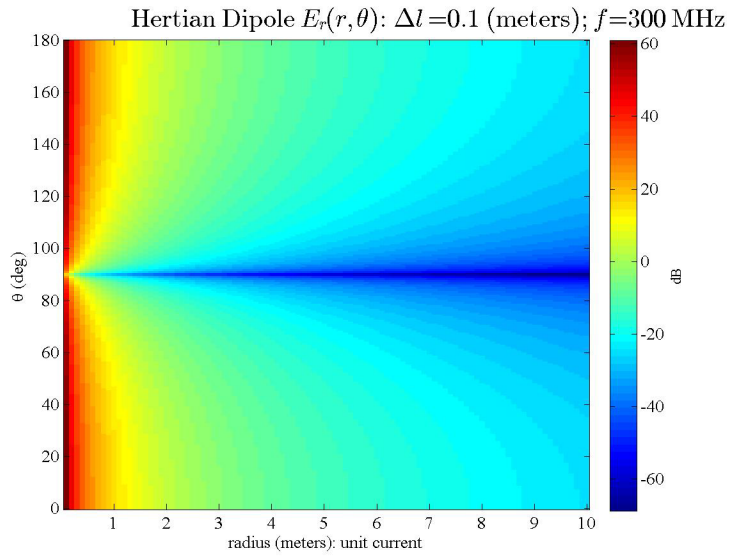
Figure 10: $|E_r(r, \theta, \phi)|$: $i_A = 1$ (A), $\lambda = 1$ (m), $\Delta\ell = \lambda/10$ (m).
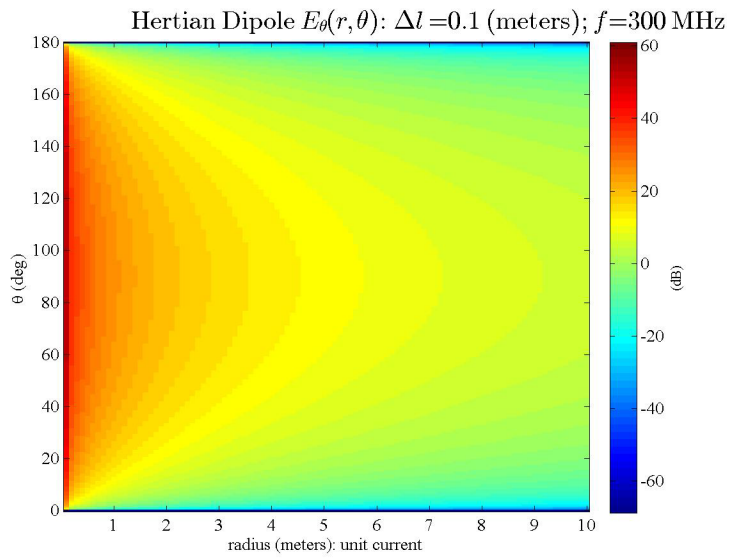
Figure 11: $|E_\theta(r, \theta, \phi)|$: $i_A = 1$ (A), $\lambda = 1$ (m), $\Delta\ell = \lambda/10$ (m).

The analysis and synthesis of this Hertzian dipole consists of sampling the fields near the antenna $(r = a)$ and recovering the far-field patterns. With

$$E_r(r, \theta, \phi) \;=\; \mathcal{O}\left[\frac{1}{(kr)^2}\right]$$

$$E_\theta(r, \theta, \phi) \;=\; \eta\frac{i_A\Delta\ell}{4\pi}k^2\sin(\theta)\exp(-jkr)\frac{j}{kr} + \mathcal{O}\left[\frac{1}{(kr)^2}\right]$$

as $r \gg a$, the *pattern function* for the electrical field is [7, Section 17.4]

$$F(\theta, \phi) := \lim_{r\to\infty} r\,\|\mathbf{E}(r, \theta, \phi)\| = \eta\frac{|i_A|\Delta\ell}{4\pi}k\sin(\theta). \tag{10}$$

4.1 Hertzian Dipole Expansions

This section uses the electric field of the Hertzian dipole to assess Sarkar's expansion in two stages. For the first stage, Sarkar's electric-field expansion is computed from the physical model of the dipole. The Hertzian dipole has electric fields (Equation 9):

$$E_0(r) \;:=\; \eta\frac{i_A\Delta\ell}{4\pi}k^2\exp(-jkr)\left\{\frac{j}{kr} + \frac{1}{(kr)^2} - \frac{j}{(kr)^3}\right\}$$

$$E_\theta(r, \theta, \phi) \;=\; E_0(r)\sin(\theta)$$

$$E_\phi(r, \theta, \phi) \;=\; 0.$$

Second, the coefficients determined by this physical model must match the coefficients computed by quadratures of the electric field measured on any near-field sphere.

The first stage will verify that the Hertzian dipole's coefficients are all zero, with the exception of

$$\alpha_{01} = -\eta k\frac{i_A\Delta\ell}{4\pi}. \tag{11}$$

Comparing the physical model with Sarkar's expansion forces the expansion in function of ϕ to vanish or that the sums collapse to $m = 0$:

$$E_\theta(r, \theta, \phi) = E_0(r)\sin(\theta)$$

$$= j\omega\mu\sum_{n=0}^{\infty}\sum_{m=0}^{n}mh_n^{(2)}(kr)\frac{P_n^m(\cos(\theta))}{\sin(\theta)}\{\gamma_{mn}\sin(m\phi) - \delta_{mn}\cos(m\phi)\}$$

$$+ \sum_{n=0}^{\infty}\sum_{m=0}^{n}\frac{1}{r}\frac{\partial}{\partial r}\left(rh_n^{(2)}(kr)\right)\frac{dP_n^m(\cos(\theta))}{d\theta}\{\alpha_{mn}\cos(m\phi) + \beta_{mn}\sin(m\phi)\}$$

$$= \sum_{n=0}^{\infty}\alpha_{0n}\frac{1}{r}\frac{\partial}{\partial r}\left(rh_n^{(2)}(kr)\right)\frac{dP_n^0(\cos(\theta))}{d\theta}$$

$$= \sum_{n=0}^{\infty}\alpha_{0n}\frac{1}{r}\frac{\partial}{\partial r}\left(rh_n^{(2)}(kr)\right)\frac{dP_n(\cos(\theta))}{d\theta},$$

15

where the P_n's are the Legendre polynomials. More precisely, $\alpha_{mn} = 0$, $\beta_{mn} = 0$, $\gamma_{mn} = 0$, $\delta_{mn} = 0$ for $m > 0$. Table 2 provides the derivatives of the Legendre polynomials to substitute into E_θ:

$$
\begin{aligned}
E_\theta(r, \theta, \phi) &= \alpha_{01} \frac{1}{r} \frac{\partial}{\partial r} \left(r h_1^{(2)}(kr) \right) P_1'(\cos(\theta))(-\sin(\theta)) \\
&\quad + \alpha_{02} \frac{1}{r} \frac{\partial}{\partial r} \left(r h_2^{(2)}(kr) \right) P_2'(\cos(\theta))(-\sin(\theta)) + \ldots \\
&= -\alpha_{01} \frac{1}{r} \frac{\partial}{\partial r} \left(r h_1^{(2)}(kr) \right) \sin(\theta) \\
&\quad - \alpha_{02} \frac{1}{r} \frac{\partial}{\partial r} \left(r h_2^{(2)}(kr) \right) 3 \cos(\theta) \sin(\theta) + \ldots .
\end{aligned}
$$

Matching the sinusoidal basis in θ gives that this electric field component expands as

$$
E_\theta(r, \theta, \phi) = -\alpha_{01} \frac{1}{r} \frac{\partial}{\partial r} \left(r h_1^{(2)}(kr) \right) \sin(\theta).
$$

The spherical Bessel term expands as

$$
\frac{1}{r} \frac{\partial}{\partial r} \left\{ r h_1^{(2)}(kr) \right\} = k \exp(-jkr) \left\{ \frac{j}{kr} + \frac{1}{(kr)^2} - \frac{j}{(kr)^3} \right\}. \tag{12}
$$

Substituting into the electric field component gives

$$
E_\theta(r, \theta, \phi) = -\alpha_{01} \sin(\theta) k \exp(-jkr) \left\{ \frac{j}{kr} + \frac{1}{(kr)^2} - \frac{j}{(kr)^3} \right\}.
$$

Comparison with the analytic formula for E_θ in Equation 9 forces the closed-form solution given in Equation 11. That is, starting with the physical model of E_θ, the Hertzian dipole's coefficients are all zero, excepting α_{01}. To complete this first stage, it is necessary to verify that this expansion explains E_ϕ using Sarkar's expansion ($\alpha_{mn} = 0$, $\beta_{mn} = 0$, $\gamma_{mn} = 0$, $\delta_{mn} = 0$ for $m > 0$): [12, Equation 6]

$$
\begin{aligned}
E_\phi(r, \theta, \phi) &= j\omega\mu \sum_{n=0}^{\infty} \sum_{m=0}^{n} h_n^{(2)}(kr) \frac{dP_n^m(\cos(\theta))}{d\theta} \{\gamma_{mn} \cos(m\phi) + \delta_{mn} \sin(m\phi)\} \\
&\quad - \sum_{n=0}^{\infty} \sum_{m=0}^{n} \frac{1}{r} \frac{\partial}{\partial r} \left(r h_n^{(2)}(kr) \right) \frac{mP_n^m(\cos(\theta))}{\sin(\theta)} \{\alpha_{mn} \sin(m\phi) - \beta_{mn} \cos(m\phi)\} \\
&= j\omega\mu \sum_{n=0}^{\infty} h_n^{(2)}(kr) \frac{dP_n(\cos(\theta))}{d\theta} \gamma_{0n} \\
&= 0,
\end{aligned}
$$

provided the γ_{mn}'s vanish entirely.

16

The second stage verifies that the coefficients in the expansion can be computed using only the electric fields measured on a given sphere. Sarkar computes α_{01} using E_θ and E_ϕ measured on a sphere of radius a whereas the expansion of the electric fields are independent of any spherical measurements. Consequently, Sarkar's formulas must cancel the measurements on the sphere. Equivalently, Sarkar's formulas must be independent of the radius:

$$\alpha_{01} = \frac{a}{kah_n^{(2)'}(ka) + h_n^{(2)}(ka)} \frac{(2n+1)(n-m)!}{2n(n+1)(n+m)!} \frac{\epsilon_m}{2\pi} \int_0^{2\pi} d\phi \int_0^\pi d\theta$$

$$\left\{ E_\theta(a,\theta,\phi) \frac{dP_n^m(\cos(\theta))}{d\theta} \sin(\theta)\cos(m\phi) - mE_\phi(a,\theta,\phi)P_n^m(\cos(\theta))\sin(m\phi) \right\}\Bigg|_{\substack{m=0 \\ n=1}}$$

$$= \frac{a}{kah_1^{(2)'}(ka) + h_1^{(2)}(ka)} \frac{3}{4} \frac{1}{2\pi} \times 2\pi \times \int_0^\pi E_\theta(a,\theta,\phi) \frac{dP_1(\cos(\theta))}{d\theta} \sin(\theta)d\theta$$

$$= \frac{a}{kah_1^{(2)'}(ka) + h_1^{(2)}(ka)} \frac{3}{4} \int_0^\pi E_\theta(a,\theta,\phi)(-\sin(\theta))\sin(\theta)d\theta$$

$$= -\frac{3}{4} \frac{a}{kah_1^{(2)'}(ka) + h_1^{(2)}(ka)} \int_0^\pi E_\theta(a,\theta)\sin(\theta)^2 d\theta.$$

Equation 12 computes the denominator:

$$kah_1^{(2)'}(ka) + h_1^{(2)}(ka) = \frac{\partial}{\partial r}\left(rh_n^{(2)}(kr)\right)\Big|_{r=a}$$

$$= \exp(-jka)\left\{ j + \frac{1}{ka} - \frac{j}{(ka)^2} \right\}.$$

On the sphere, the electric field

$$E_\theta(a,\theta) = \eta \frac{i_A \Delta\ell}{4\pi} \frac{k}{a} \sin(\theta)\exp(-jka)\left\{ j + \frac{1}{ka} - \frac{j}{(ka)^2} \right\}$$

integrates as

$$\int_0^\pi E_\theta(a,\theta)\sin(\theta)^2 d\theta = \eta \frac{i_A \Delta\ell}{4\pi} \frac{k}{a} \exp(-jka)\left\{ j + \frac{1}{ka} - \frac{j}{(ka)^2} \right\} \int_0^\pi \sin(\theta)^3 d\theta$$

$$= \eta \frac{i_A \Delta\ell}{4\pi} \frac{k}{a} \exp(-jka)\left\{ j + \frac{1}{ka} - \frac{j}{(ka)^2} \right\} \times \frac{4}{3}.$$

Combining the numerator and denominator

$$
\begin{aligned}
\alpha_{01} &= -\frac{3}{4} \frac{a}{ka h_1^{(2)'}(ka) + h_1^{(2)}(ka)} \int_0^\pi E_\theta(a,\theta) \sin(\theta)^2 d\theta \\
&= -\frac{3}{4} \frac{a}{\exp(-jka)\left\{ j + \frac{1}{ka} - \frac{j}{(ka)^2} \right\}} \eta \frac{i_A \Delta \ell}{4\pi} \frac{k}{a} \\
&\quad \times \exp(-jka)\left\{ j + \frac{1}{ka} - \frac{j}{(ka)^2} \right\} \times \frac{4}{3} \\
&= -\eta k \frac{i_A \Delta \ell}{4\pi}.
\end{aligned}
$$

Consequently, Sarkar's denominator term cancels the effect of the radius a in the measured electric field to produce an α_{01} that is independent of the measuring sphere.

18

4.2   Hertzian Dipole Quadratures

The Hertzian dipole has electric fields (Equation 9):

$$
\begin{aligned}
E_0(r) &:= \eta \frac{i_A \Delta \ell}{4\pi} k^2 \exp(-jkr) \left\{ \frac{j}{kr} + \frac{1}{(kr)^2} - \frac{j}{(kr)^3} \right\}, \\
E_\theta(r, \theta, \phi) &= E_0(r) \sin(\theta), \\
E_\phi(r, \theta, \phi) &= 0.
\end{aligned}
$$

Figure 12 plots the magnitude of E_θ on the sphere $a = 3\lambda$ over the angular grid sampled at $18°$ increments.
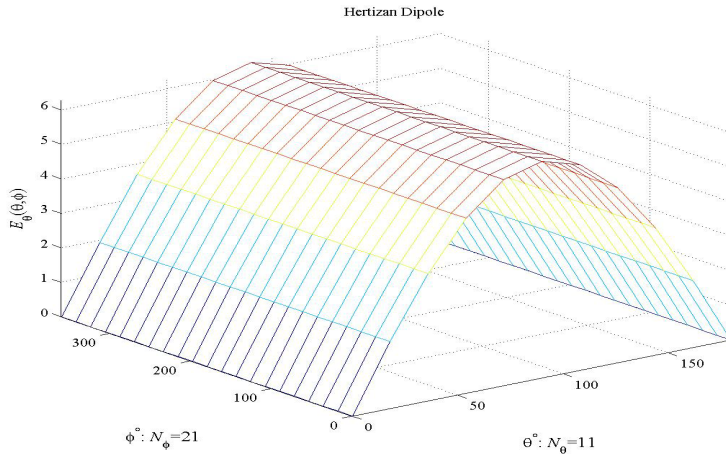
Figure 12: Hertzian dipole $|E_\theta(a, \theta, \phi)|$; $i_A = 1$ amp, $\lambda = 1$ meter, $\Delta \ell = \lambda/10$ meter; $a = 3\lambda, \Delta\theta = 18°$, $\Delta\phi = 18°$.

The Hertzian dipole has only the single non-zero coefficient given by Equation 11:

$$
\alpha_{01} = -\eta k \frac{i_A \Delta \ell}{4\pi} = -18.8496,
$$

where the numerical value is computed using the parameters in Figure 12. Tables 3 and 4 report on the coefficients α_{mn} estimated from the sampled values on the sphere $a = 3\lambda$. The real part of these α_{mn}'s is accurate to 5 places whereas the imaginary part is accurate to 6 places.

Tables 3 and 4 compute the α_{mn} from the electric fields sampled on a sphere of fixed radius $a = 3\lambda$. Figure 13 displays the effect of varying the sampling radius. The accuracy remains at 5 places for $\lambda \leq a \leq 5\lambda$. This stability of α_{01} as a function of the sampling radius provides a partial answer to the question of Section 1. The near-to-far transformation is stable for near-fields of the ideal dipole where the sampling sphere ranges as $\lambda \leq a \leq 5\lambda$.

19

Table 3: $\Re(\alpha_{mn})$ estimated from E_θ and E_ϕ sampled on the sphere $a = 3\lambda$.

	$n = 1$	$n = 2$	$n = 3$
$m = 0$	-18.84930	0.00000	-0.00000
$m = 1$	0.00000	0.00000	-0.00000
$m = 2$		-0.00000	-0.00000
$m = 3$			-0.00000

Table 4: $\Im(\alpha_{mn})$ estimated from E_θ and E_ϕ sampled on the sphere $a = 3\lambda$.

	$n = 1$	$n = 2$	$n = 3$
$m = 0$	$-1.11 \cdot 10^{-15}$	$-1.11 \cdot 10^{-15}$	$-1.18 \cdot 10^{-6}$
$m = 1$	$2.36 \cdot 10^{-17}$	$-5.95 \cdot 10^{-11}$	$-1.63 \cdot 10^{-16}$
$m = 2$		$8.75 \cdot 10^{-16}$	$-5.65 \cdot 10^{-10}$
$m = 3$			$-1.32 \cdot 10^{-15}$
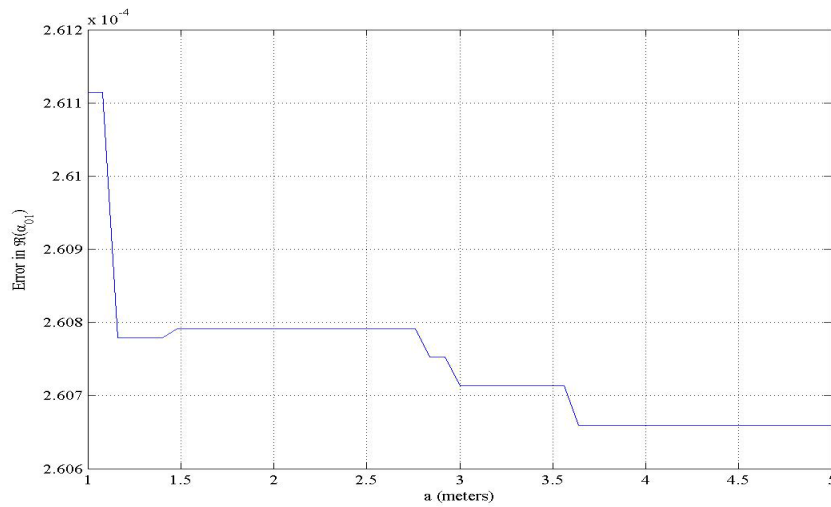
Figure 13: Hertzian dipole: error in $\Re(\alpha_{01})$ as a function of the sampling sphere.

4.3 Hertzian Dipole Synthesis

Once the spherical coefficients are computed from measurement on a sphere of radius $r = a$, Sarkar's expansions compute the electric field at distances $r \geq a$. This section verifies that the sampled electric field can be recovered on the measurement sphere.

Figure 14 reports on the expansion of $E_\theta(r, \theta, \phi)$ at $r = a$ using the numerical coefficients in Tables 3 and 4. Comparison with the analytic $E_\theta(a, \theta, \phi)$ in Figure 12 shows credible agreement. In the notation of Section 2, the synthetic $E_\theta(a, \theta, \phi)$ computed using Sarkar's expansion is a credible approximation despite the truncation ($N = 3$) and discretization ($\Delta\theta = 18°$, $\Delta\phi = 18°$):

$$E_\theta(a, \theta, \phi) \approx \mathfrak{S}(a = 3; \Delta\theta = 18°, \Delta\phi = 18°, N = 3; a, \theta, \phi).$$
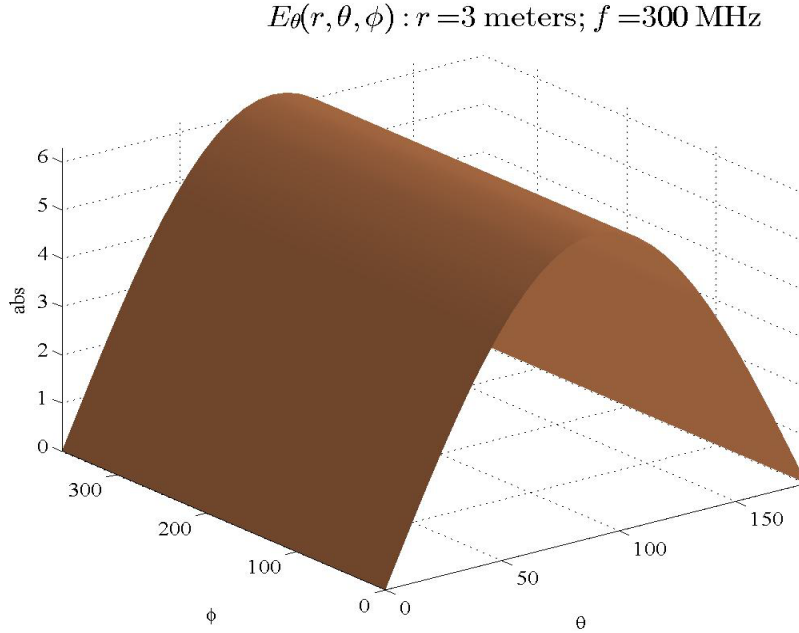
Figure 14: Synthesis of $E_\theta(a, \theta, \phi)$ with $m \leq n \leq 3$.

Likewise, Figure 15 reports on the expansion at $E_\phi(r, \theta, \phi)$ at $r = a$ using the numerical coefficients in Tables 3 and 4. Because $E_\phi(r, \theta, \phi) = 0$, the absolute error is approximately $1.2 \cdot 10^{-7}$.

$$E_\phi(r, \theta, \phi) : r = 3 \text{ meters}; f = 300 \text{ MHz}$$
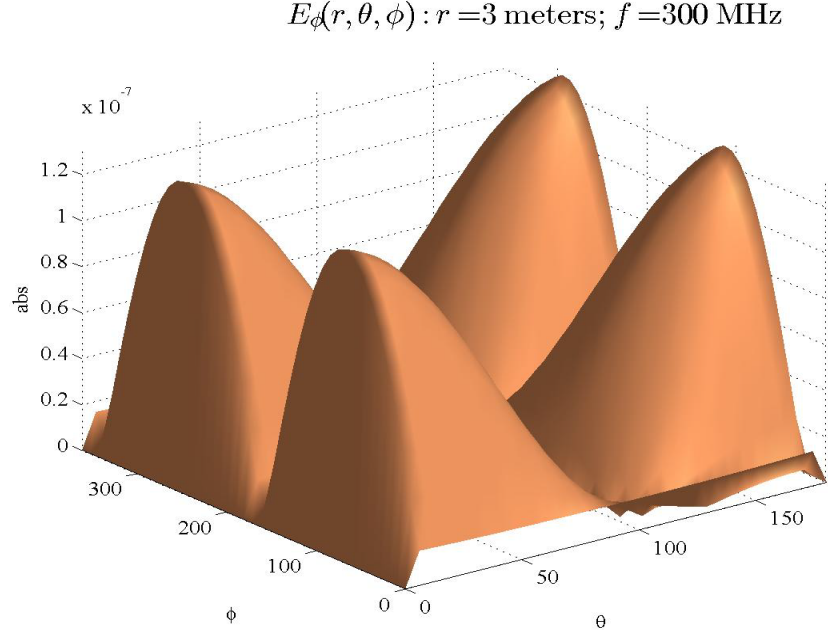
Figure 15: Synthesis of $E_\phi(a, \theta, \phi)$ with $m \leq n \leq 3$.

4.4   Hertzian Dipole in the Far Field

The last step in Sarkar's near-to-far transformation is to take the coefficients computed in the near field and synthesize the far-field pattern. Figure 16 shows $E_\theta(r, \theta, \phi)$ in the r-θ plane out to $r = 100\lambda$. Figure 17 shows the corresponding image of the synthesized $E_\theta(r, \theta, \phi)$ determined by the synthesis code. The synthesis code implements Sarkar's expansion given the coefficients α, β, γ, and δ. This code was tested by inserting the exact value of the coefficients. That is, all coefficients are zeros excepting $\alpha_{01} = -18.8496$ set by Equation 11. Comparison of both figures shows that the magnitude of the synthesized electric field is a credible approximation to the analytic field.
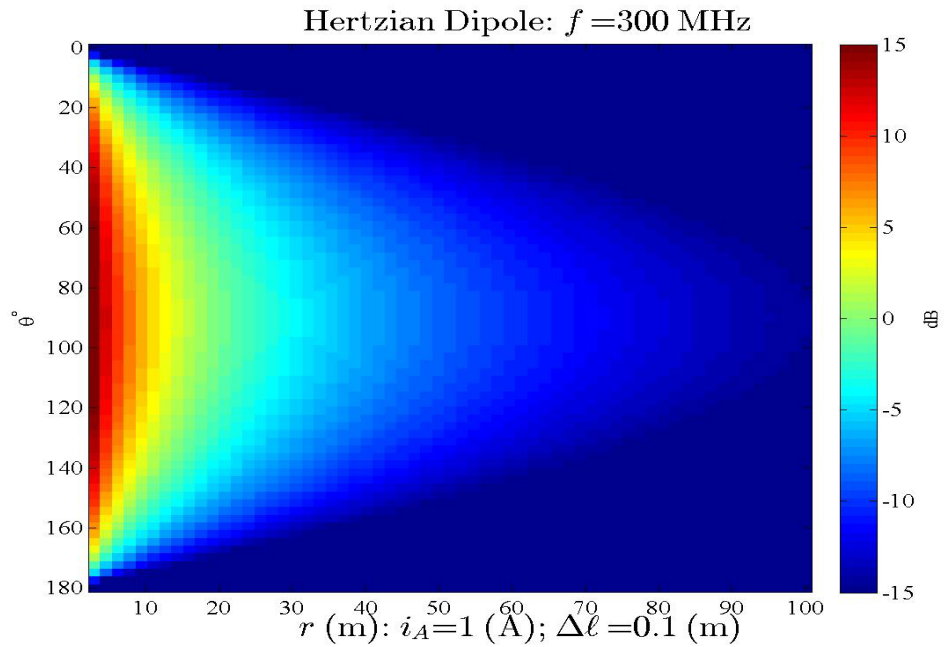
Figure 16: Exact $E_\theta(r, \theta, \phi)$.
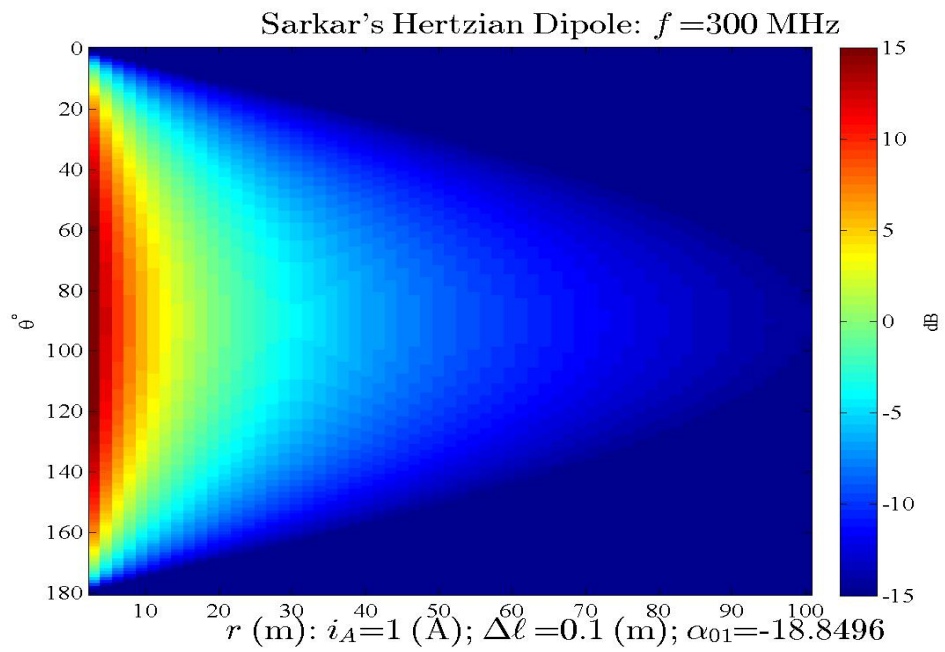
Figure 17: Synthetic $E_\theta(r, \theta, \phi)$.

23

The far-field pattern function for the electric field is given in Equation 10 and repeated here for convenience:

$$F(\theta, \phi) := \lim_{r \to \infty} r \, \|\mathbf{E}(r, \theta, \phi)\| = \eta \frac{|i_A| \Delta \ell}{4\pi} k \sin(\theta).$$

Figure 18 compares this pattern function against two approximations. The approximation labeled "Exact" is $r|E_\theta(r, \theta, \phi)|$ evaluated at $r = 100$ m. The approximation labeled "Synthetic" is the corresponding computation using the synthesis code. The approximations are relatively close to the true pattern.
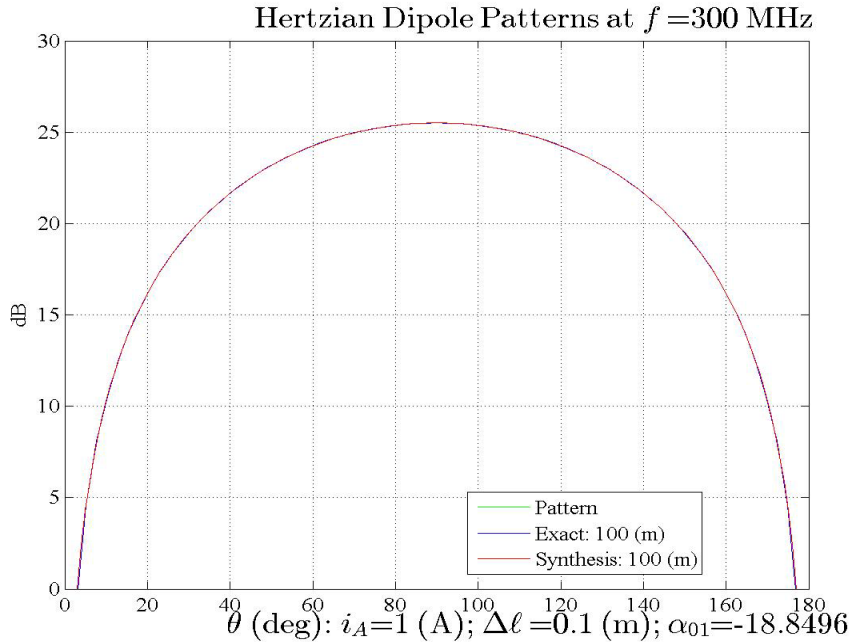
Figure 18: Far-field pattern comparison: $i_A = 1$ A(A), $\lambda = 1$ (m), $\Delta \ell = \lambda/10$ (m).

5   The Small Loop Antenna

The Hertzian dipole's computations required only E_θ because E_ϕ is zero. A loop antenna tests the near-to-far transformation when E_ϕ is non-zero and E_θ is zero. The electric field for a small loop antenna is [4, Equation 5-19]

$$
\begin{aligned}
E_r(r, \theta, \phi) &= 0 \\
E_\theta(r, \theta, \phi) &= 0 \\
E_\phi(r, \theta, \phi) &= \eta \frac{i_A \Delta S}{4\pi} k^3 \sin(\theta) \exp(-jkr) \left\{ \frac{1}{kr} - \frac{j}{(kr)^2} \right\},
\end{aligned}
\qquad (13)
$$

where $\Delta S = \pi r_\ell^2$ is the area of the loop. This electric field expanded and synthesized to assess Sarkar's expansion.

5.1   Expansions

This analytic form of the electric field determines the coefficients of Sarkar's expansion. Sarkar's expansion for E_ϕ is repeated here for convenience: [12, Equation 6]

$$
\begin{aligned}
E_\phi(r, \theta, \phi) = {}& j\omega\mu \sum_{n=0}^{\infty} \sum_{m=0}^{n} h_n^{(2)}(kr) \frac{dP_n^m(\cos(\theta))}{d\theta} \{\gamma_{mn} \cos(m\phi) + \delta_{mn} \sin(m\phi)\} \\
& - \sum_{n=0}^{\infty} \sum_{m=0}^{n} \frac{1}{r} \frac{\partial}{\partial r} \left(r h_n^{(2)}(kr) \right) \frac{m P_n^m(\cos(\theta))}{\sin(\theta)} \{\alpha_{mn} \sin(m\phi) - \beta_{mn} \cos(m\phi)\}.
\end{aligned}
$$

The symmetry of E_ϕ with respect to ϕ forces the sums to collapse to $m = 0$:

$$
E_\phi(r, \theta, \phi) = j\omega\mu \sum_{n=0}^{\infty} h_n^{(2)}(kr) \frac{dP_n(\cos(\theta))}{d\theta} \gamma_{0n}.
$$

More precisely, this expansion forces $\alpha_{mn} = 0$, $\beta_{mn} = 0$, $\gamma_{mn} = 0$, and $\delta_{mn} = 0$ for $m > 0$. Consequently, the expansion for E_θ must take the form [12, Equation 5]:

$$
\begin{aligned}
E_\theta(r, \theta, \phi) = {}& j\omega\mu \sum_{n=0}^{\infty} \sum_{m=0}^{n} m h_n^{(2)}(kr) \frac{P_n^m(\cos(\theta))}{\sin(\theta)} \{\gamma_{mn} \sin(m\phi) - \delta_{mn} \cos(m\phi)\} \\
& + \sum_{n=0}^{\infty} \sum_{m=0}^{n} \frac{1}{r} \frac{\partial}{\partial r} \left(r h_n^{(2)}(kr) \right) \frac{dP_n^m(\cos(\theta))}{d\theta} \{\alpha_{mn} \cos(m\phi) + \beta_{mn} \sin(m\phi)\} \\
= {}& \sum_{n=0}^{\infty} \frac{1}{r} \frac{\partial}{\partial r} \left(r h_n^{(2)}(kr) \right) \frac{dP_n^0(\cos(\theta))}{d\theta} \alpha_{0n}.
\end{aligned}
$$

The vanishing $E_\theta = 0$ forces $\alpha_{mn} = 0$ for all m, $n \geq 0$. Returning to the expansion of E_ϕ, the product of the radial term and elevation term for $n = 1$ is

$$
\begin{aligned}
h_1^{(2)}(kr)\frac{dP_1(\cos(\theta))}{d\theta} &= \exp(-jr)\left\{-\frac{1}{r} + \frac{j}{r^2}\right\}(-\sin(\theta)) \\
&= \sin(\theta)\exp(-jr)\left\{\frac{1}{r} - \frac{j}{r^2}\right\}.
\end{aligned}
$$

Comparison with the physical model of E_ϕ of Equation 13 forces all γ_{0n}'s to zero with the exception

$$
\begin{aligned}
E_\phi(r, \theta, \phi) &= \eta\frac{i_A\Delta S}{4\pi}k^3\left\{h_1^{(2)}(kr)\frac{dP_1(\cos(\theta))}{d\theta}\right\} \\
&= j\omega\mu h_1^{(2)}(kr)\frac{dP_1(\cos(\theta))}{d\theta}\gamma_{01}.
\end{aligned}
$$

That is, the physical model of the small loop antenna forces

$$
j\omega\mu\gamma_{01} = \eta\frac{i_A\Delta S}{4\pi}k^3.
$$

For convenience, recall that [5, Equation 9-14], [5, Equation 9-28], [5, Equation 10-33]:

$$
c_0 = \frac{1}{\sqrt{\epsilon\mu}}, \quad \eta = \sqrt{\frac{\mu}{\epsilon}}, \quad k = \frac{\omega}{c_0}.
$$

Solving for the coefficient

$$
\begin{aligned}
\gamma_{01} &= \frac{1}{j}\frac{\eta}{\mu}\frac{i_A\Delta S}{4\pi}\frac{k^3}{\omega} \\
&= -j\frac{1}{\sqrt{\mu\epsilon}}\frac{i_A\Delta S}{4\pi}\frac{k^2}{c_0} \\
&= -jc_0\frac{i_A\Delta S}{4\pi}\frac{k^2}{c_0} \\
&= -j\frac{i_A\Delta S}{4\pi}k^2.
\end{aligned}
$$

That is, the small loop's coefficients are all zero, excepting

$$
\gamma_{01} = -j\frac{i_A\Delta S}{4\pi}k^2. \tag{14}
$$

The second task is to verify that the coefficients in the expansion can be computed using only the electric fields measured on a given sphere. Sarkar computes γ_{01} using E_θ and E_ϕ measured on a sphere of radius a whereas the expansion of the electric fields

are independent of any spherical measurements. Consequently, Sarkar's formulas must cancel the measurements on the sphere. Equivalently, Sarkar's formulas must be independent of the radius:

$$
\begin{aligned}
\gamma_{01} &= \frac{1}{j\omega\mu h_n^{(2)}(ka)} \frac{(2n+1)(n-m)!}{2n(n+1)(n+m)!} \frac{\epsilon_m}{2\pi} \int_0^{2\pi} d\phi \int_0^{\pi} d\theta \\
&\quad \left\{ E_\phi(a,\theta,\phi) \frac{dP_n^m(\cos(\theta))}{d\theta} \sin(\theta)\cos(m\phi) + mE_\theta(a,\theta,\phi)P_n^m(\cos(\theta))\sin(m\phi) \right\} \Bigg|_{\substack{m=0 \\ n=1}} \\
&= \frac{1}{j\omega\mu h_1^{(2)}(ka)} \frac{3}{4} \frac{1}{2\pi} \int_0^{2\pi} d\phi \int_0^{\pi} d\theta E_\phi(a,\theta,\phi) \frac{dP_1^0(\cos(\theta))}{d\theta} \sin(\theta) \\
&= \frac{1}{j\omega\mu h_1^{(2)}(ka)} \frac{3}{4} \int_0^{\pi} E_\phi(a,\theta,\phi) \left\{ \frac{d}{d\theta}\cos(\theta) \right\} \sin(\theta)\, d\theta \\
&= -\frac{1}{j\omega\mu h_1^{(2)}(ka)} \frac{3}{4} \int_0^{\pi} E_\phi(a,\theta,\phi) \sin(\theta)^2\, d\theta \\
&= -\frac{1}{j\omega\mu h_1^{(2)}(ka)} \eta \frac{i_A\Delta S}{4\pi} k^3 \exp(-jka) \left\{ \frac{1}{ka} - \frac{j}{(ka)^2} \right\} \frac{3}{4} \int_0^{\pi} \sin(\theta)^3\, d\theta \\
&= -\frac{1}{j\omega\mu h_1^{(2)}(ka)} \eta \frac{i_A\Delta S}{4\pi} k^3 (-h_1^{(2)}(ka)) \\
&= \frac{\eta k^3}{j\omega\mu} \frac{i_A\Delta S}{4\pi} \\
&= -jk^2 \frac{i_A\Delta S}{4\pi}.
\end{aligned}
$$

That is, γ_{01} determined by the small loop's physical model (Equation 14) may also be computed by a quadrature that integrates the electric fields measured over a sphere.

5.2 Quadratures

The small loop antenna has electric fields $E_\theta(r, \theta, \phi) = 0$ and

$$E_\phi(r, \theta, \phi) = \eta \frac{i_A \Delta S}{4\pi} k^3 \sin(\theta) \exp(-jkr) \left\{ \frac{1}{kr} - \frac{j}{(kr)^2} \right\},$$

where $\Delta S = \pi r_\ell^2$ is the area of the loop. Figure 19 plots the magnitude of E_ϕ on the sphere $a = 3\lambda$ over the angular grid sampled at 18° increments.
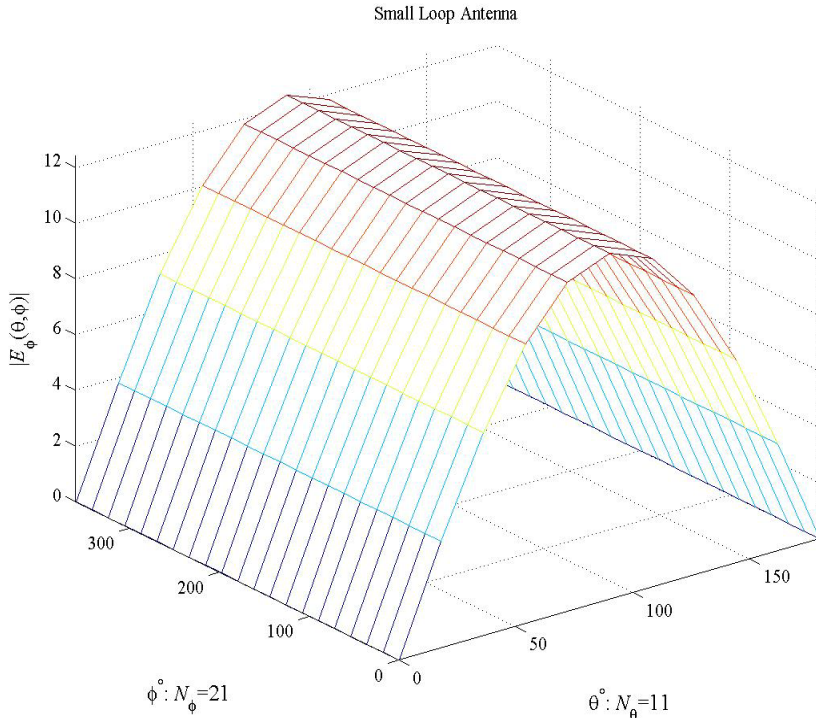
Figure 19: $|E_\phi(a, \theta, \phi)|$ of the small loop antenna; $i_A = 1$ amp, $\lambda = 1$ meter, $r_\ell = \lambda/10$ meter; $a = 3\lambda$, $\Delta\theta = 18°$, $\Delta\phi = 18°$.

The small loop antenna has only the single non-zero coefficient given by Equation 14:

$$\gamma_{01} = -j \frac{i_A \Delta S}{4\pi} k^2 = -j0.098696,$$

where the numerical value is computed using the parameters in Figure 19. Tables 5 and 6 report the coefficients γ_{mn} estimated from the sampled values on the sphere $a = 3\lambda$. The real part of these γ_{mn}'s is accurate to 9 places whereas the imaginary part is accurate to 5 places. Figure 20 displays the effect of varying the sampling radius. The accuracy remains at five decimal places for $\lambda \leq a \leq 5\lambda$. This stability

28

Table 5: $\Re(\gamma_{mn})$ estimated from E_θ and E_ϕ sampled on the sphere $a = 3\lambda$

	$n = 1$	$n = 2$	$n = 3$
$m = 0$	$1.65 \cdot 10^{-17}$	$4.36 \cdot 10^{-18}$	$6.07 \cdot 10^{-9}$
$m = 1$	$1.34 \cdot 10^{-20}$	$-3.66 \cdot 10^{-12}$	$-4.40 \cdot 10^{-20}$
$m = 2$		$-9.34 \cdot 10^{-20}$	$-3.04 \cdot 10^{-15}$
$m = 3$			$6.20 \cdot 10^{-21}$

Table 6: $\Im(\gamma_{mn})$ estimated from E_θ and E_ϕ sampled on the sphere $a = 3\lambda$

	$n = 1$	$n = 2$	$n = 3$
$m = 0$	-0.098695	0.000000	-0.000000
$m = 1$	-0.000000	-0.000000	0.000000
$m = 2$		-0.000000	0.000000
$m = 3$			-0.000000

of γ_{01} as a function of the sampling radius provides a partial answer to the question of Section 1—the near-to-far transformation is stable for the near-fields of the small loop antenna where the sampling sphere ranges as $\lambda \leq a \leq 5\lambda$.
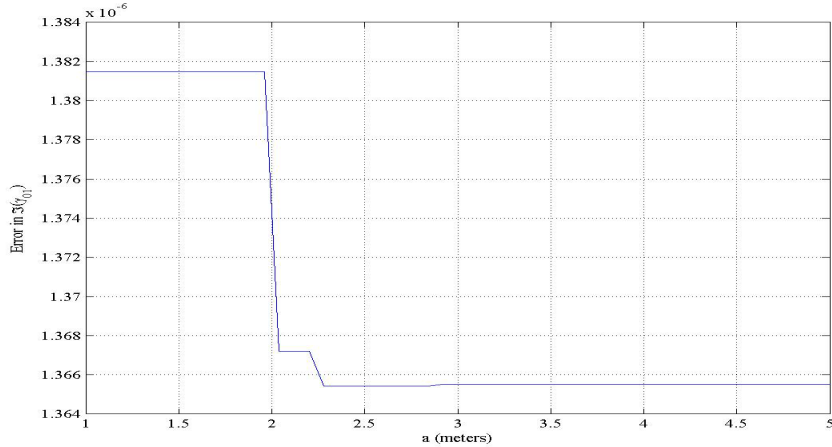
Figure 20: Small Loop Antenna: error in $\Im(\gamma_{01})$ as a function of the sampling sphere.

29

5.3 Synthesis

Synthesis uses the coefficients estimated by the quadratures to reconstruct the fields of the small loop antenna. Figure 21 plots E_ϕ synthesized from the estimated coefficients using only the relatively coarse sampling of the E_ϕ and $E_\theta = 0$ fields. The shape and peak values are in agreement with Figure 19.

$$E_\phi(r, \theta, \phi) : r = 3 \text{ meters}; \ f = 300 \text{ MHz}$$
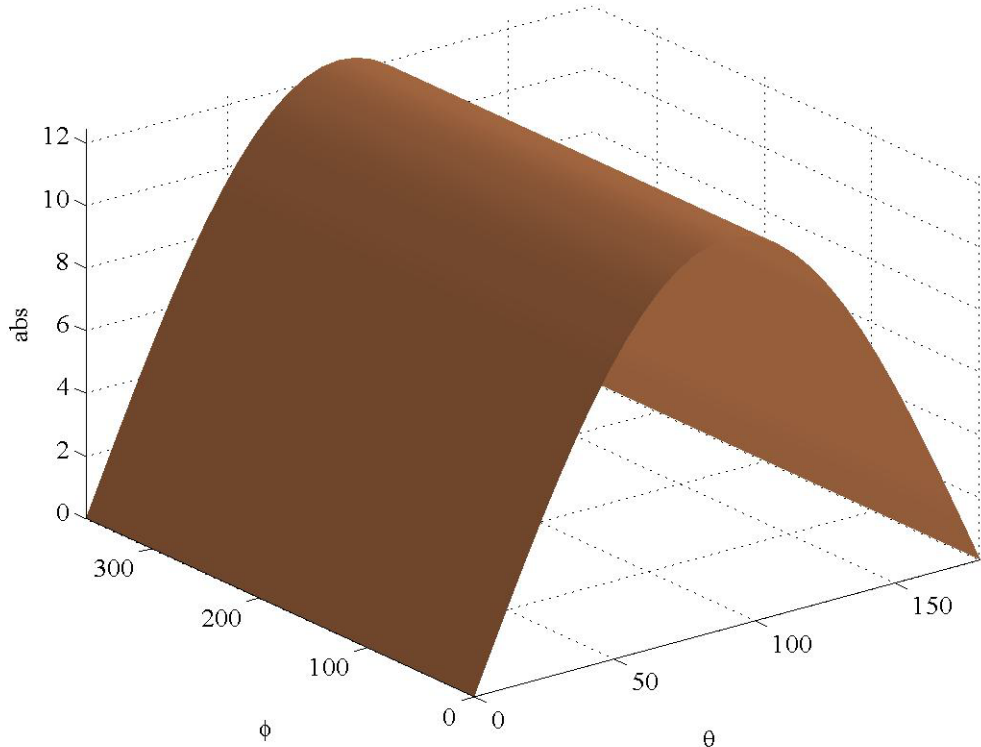
Figure 21: Small Loop Synthesis $|E_\phi(a, \theta, \phi)|$; $i_A = 1$ amp, $\lambda = 1$ meter, $r_\ell = \lambda/10$ meter; $a = 3\lambda$, $\Delta\theta = 18°$, $\Delta\phi = 18°$.

5.4   Far-Field Pattern

This section compares the exact far-field patterns of the small loop antenna to the synthesized patterns. Figure 22 plots E_ϕ as a function of range r and angle θ from Equation 13. Figure 23 plots E_ϕ generated using the synthesis code with the exact values for Sarkar's coefficients: α, β, γ, and δ are all zero excepting $\gamma_{01} = -j0.098696$. These slices of the exact and synthetic electric field verify that the synthesis is accurate for this antenna.
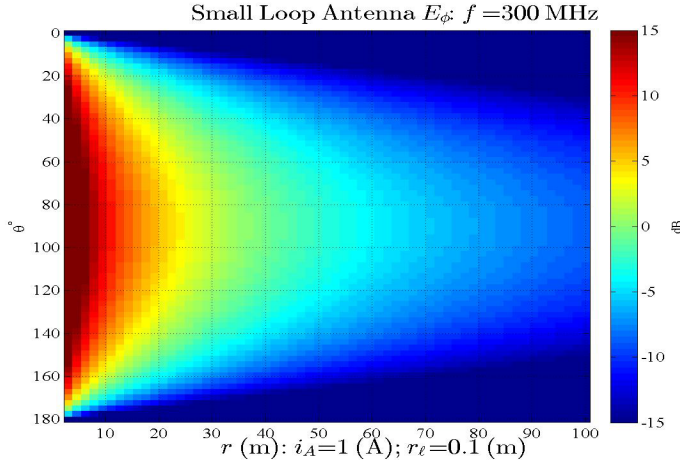
Figure 22: Small Loop Antenna $|E_\phi(r, \theta, \phi)|$.
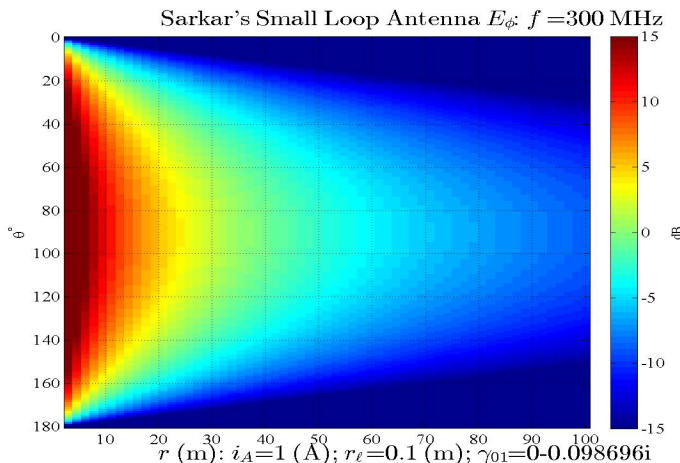
Figure 23: Synthetic $|E_\phi(r, \theta, \phi)|$.

The pattern function for the small loop antenna is obtained from Equation 13:

$$F(\theta, \phi) = \lim_{r \to \infty} r \|\mathbf{E}(r, \theta, \phi)\| = \eta \frac{|i_A| \Delta S}{4\pi} k^2 \sin(\theta).$$

Figure 24 compares this pattern function against two approximations. The approximation labeled "Exact" is $r|E_\theta(r, \theta, \phi)|$ evaluated at $r = 100$ m. The approximation labeled "Synthetic" is the corresponding computation using the synthesis code. The approximations are relatively close to the small loop pattern.
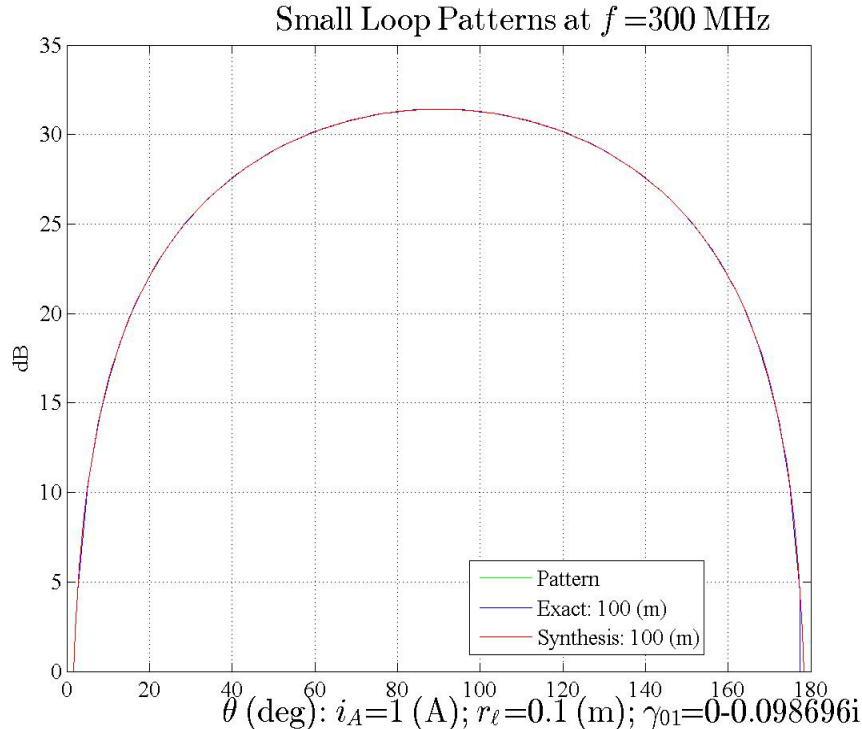
Figure 24: Far-field pattern comparison: $i_A = 1$ (A), $\lambda = 1$ (m), $r_\ell = \lambda/10$ (m).

32

6 A Synthetic α Field

Define a synthetic electric field with $\alpha_{11} = 1$ as the only non-zero coefficient. The angular components of the electric field are

$$
\begin{aligned}
E_\theta(r,\theta,\phi) &= +\frac{1}{r}\frac{\partial}{\partial r}\left(rh_1^{(2)}(kr)\right)\frac{dP_1^1(\cos(\theta))}{d\theta}\cos(\phi) \\
E_\phi(r,\theta,\phi) &= -\frac{1}{r}\frac{\partial}{\partial r}\left(rh_1^{(2)}(kr)\right)\frac{P_1^1(\cos(\theta))}{\sin(\theta)}\sin(\phi).
\end{aligned}
$$

Use [3, Table 12.3 with footnote]

$$
P_1^1(\cos(\theta)) = -\sin(\theta) \implies \frac{dP_1^1(\cos(\theta))}{d\theta} = -\cos(\theta).
$$

Use [3, Equation 11.150]:

$$
h_1^{(2)}(r) = \exp(-jr)\left\{-\frac{1}{r}+\frac{j}{r^2}\right\}
$$

to compute

$$
\begin{aligned}
\frac{1}{r}\frac{\partial}{\partial r}\left(rh_1^{(2)}(kr)\right) &= \frac{1}{r}\frac{\partial}{\partial r}\left(rh_1^{(2)}(kr)\right) \\
&= \exp(-jkr)\left\{\frac{j}{r}+\frac{1}{kr^2}-\frac{j}{k^2r^3}\right\} \\
&= \exp(-jkr)k\left\{\frac{j}{kr}+\frac{1}{(kr)^2}-\frac{j}{(kr)^3}\right\} \\
&=: E_0(r).
\end{aligned}
$$

The electric field forced by $\alpha_{11} = 1$ has the form:

$$
\begin{aligned}
E_\theta(r,\theta,\phi) &= -E_0(r)\cos(\theta)\cos(\phi) \\
E_\phi(r,\theta,\phi) &= +E_0(r)\sin(\phi).
\end{aligned}
$$

Figure 25 reports the electric field and the resulting synthesis. The upper panels are sampled using $N_\phi = 73$ and $N_\theta = 43$ sample points for a angular grid size of $\Delta\phi = 5°$ and $\Delta\theta = 4.3°$. Only these sample values are input to the analysis code to estimate Sarkar's coefficients. The lower panels show the resulting synthesis. Comparison of the upper panels and lower panels shows that the magnitude of the synthesized electric is a credible approximation to the sampled field.
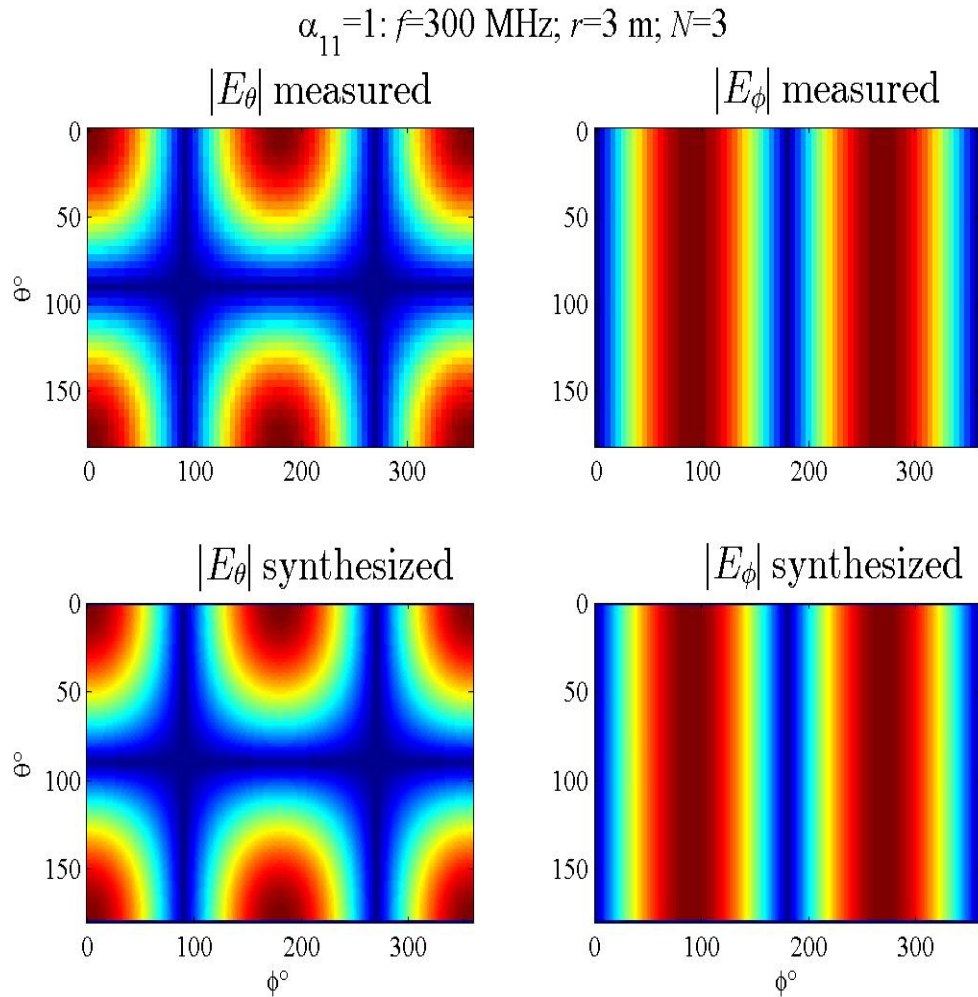
Figure 25: Synthesis of the $\alpha_{11} = 1$ field.

The electric field was synthesized in the preceding plots. However, there is the question if the electric field determined by the α_{11} is represented by this single term.

Question: Is α_{11} the only non-zero coefficient of this electric field?

The following analysis answers this question positively and leads to the second question regarding the numerical quadrature.

Question: How well does the numerical quadrature estimate α_{11} compare to the vanishing coefficients of this electric field?

The β_{mn}'s vanish because of the orthogonality between $\cos(\phi)$ and $\sin(\phi)$ and the basis functions $\sin(m\phi)$ and $\cos(m\phi)$, respectively.

$$\beta_{mn} = \frac{a}{kah_n^{(2)\prime}(ka) + h_n^{(2)}(ka)} \frac{(2n+1)(n-m)!}{2n(n+1)(n+m)!} \frac{\epsilon_m}{2\pi} \{b_{\phi;mn} + b_{\theta;mn}\}.$$

Integrating each term separately,

$$
\begin{aligned}
b_{\phi;mn} &= \int_0^{2\pi} d\phi \int_0^{\pi} d\theta \ mE_\phi(a,\theta,\phi)P_n^m(\cos(\theta))\cos(m\phi) \\
&= \int_0^{2\pi} d\phi \int_0^{\pi} d\theta \ m\{E_0(r)\sin(\phi)\}P_n^m(\cos(\theta))\cos(m\phi) \\
&= mE_0(r)\int_0^{2\pi} \sin(\phi)\cos(m\phi)d\phi \int_0^{\pi} P_n^m(\cos(\theta))d\theta \\
&= 0
\end{aligned}
$$

$$
\begin{aligned}
b_{\theta;mn} &= \int_0^{2\pi} d\phi \int_0^{\pi} d\theta \ E_\theta(a,\theta,\phi)\frac{dP_n^m(\cos(\theta))}{d\theta}\sin(\theta)\sin(m\phi) \\
&= -E_0(r)\int_0^{2\pi} d\phi \int_0^{\pi} d\theta \ \{\cos(\theta)\cos(\phi)\}\frac{dP_n^m(\cos(\theta))}{d\theta}\sin(\theta)\sin(m\phi) \\
&= -E_0(r)\int_0^{2\pi} \cos(\phi)\sin(m\phi)d\phi \int_0^{\pi} \frac{dP_n^m(\cos(\theta))}{d\theta}\sin(\theta)\cos(\theta)d\theta \\
&= 0.
\end{aligned}
$$

Thus, the β_{mn}'s must vanish in a credible quadrature. Table 7 reports the quadrature computations β_{mn} from Figure 25. These coefficients vanish nearly to the machine ϵ.

The δ_{mn}'s vanish mainly because the orthogonality of the sinusoids, excepting for $m = 1$.

$$\delta_{mn} = \frac{1}{j\omega\mu h_n^{(2)}(ka)} \frac{(2n+1)(n-m)!}{2n(n+1)(n+m)!} \frac{\epsilon_m}{2\pi} \{d_{\phi,mn} - d_{\theta,mn}\}.$$

Table 7: $|\beta_{mn}|$ estimated from E_θ and E_ϕ sampled on the sphere $a = 3\lambda$.

	$n = 1$	$n = 2$	$n = 3$
$m = 0$	0	0	
$m = 1$	$4.12 \cdot 10^{-17}$	$9.51 \cdot 10^{-19}$	$9.17 \cdot 10^{-18}$
$m = 2$		$2.90 \cdot 10^{-17}$	$1.08 \cdot 10^{-18}$
$m = 3$			$2.47 \cdot 10^{-18}$

$$
\begin{aligned}
d_{\phi;mn} &= \int_0^{2\pi} d\phi \int_0^\pi d\theta \, E_\phi(a,\theta,\phi) \frac{dP_n^m(\cos(\theta))}{d\theta} \sin(\theta) \sin(m\phi) \\
&= \int_0^{2\pi} d\phi \int_0^\pi d\theta \, \{E_0(r)\sin(\phi)\} \frac{dP_n^m(\cos(\theta))}{d\theta} \sin(\theta) \sin(m\phi) \\
&= E_0(r) \int_0^{2\pi} \sin(\phi)\sin(m\phi)d\phi \int_0^\pi \frac{dP_n^m(\cos(\theta))}{d\theta} \sin(\theta)d\theta \\
&= E_0(r)\pi\chi(m=1) \int_0^\pi \frac{dP_n^1(\cos(\theta))}{d\theta} \sin(\theta)d\theta \\
&\overset{\text{by parts}}{=} E_0(r)\pi\chi(m=1) \left\{ P_m^1(\cos(\theta))\sin(\theta)\big|_0^\pi - \int_0^\pi \cos(\theta)P_n^1(\cos(\theta))d\theta \right\} \\
&= -E_0(r)\pi\chi(m=1) \int_0^\pi \cos(\theta)P_n^1(\cos(\theta))d\theta.
\end{aligned}
$$

For the contribution of the elevation components,

$$
\begin{aligned}
d_{\theta;mn} &= \int_0^{2\pi} d\phi \int_0^\pi d\theta \, mE_\theta(a,\theta,\phi)P_n^m(\cos(\theta))\cos(m\phi) \\
&= m\int_0^{2\pi} d\phi \int_0^\pi d\theta \, \{-E_0(r)\cos(\theta)\cos(\phi)\}P_n^m(\cos(\theta))\cos(m\phi) \\
&= mE_0(r) \int_0^{2\pi} \cos(\phi)\cos(m\phi)d\phi \int_0^\pi \cos(\theta)P_n^m(\cos(\theta))d\theta \\
&= mE_0(r)\pi\chi(m=1) \int_0^\pi \cos(\theta)P_n^1(\cos(\theta))d\theta \\
&= E_0(r)\pi\chi(m=1) \int_0^\pi \cos(\theta)P_n^1(\cos(\theta))d\theta.
\end{aligned}
$$

Therefore, $d_{\phi;mn} - d_{\theta;mn} = 0$ and the δ_{mn}'s must also vanish. Table 8 reports the quadrature computations δ_{mn} from Figure 25. These coefficients vanish nearly to the machine ϵ, with the exception of δ_{12}.

Table 8: $|\delta_{mn}|$ estimated from E_θ and E_ϕ sampled on the sphere $a = 3\lambda$.

	$n = 1$	$n = 2$	$n = 3$
$m = 0$	0	0	0
$m = 1$	$1.82 \cdot 10^{-19}$	$3.89 \cdot 10^{-8}$	$9.76 \cdot 10^{-20}$
$m = 2$		$9.01 \cdot 10^{-22}$	$9.73 \cdot 10^{-11}$
$m = 3$			$6.28 \cdot 10^{-22}$

Tables 9 and 10 report the magnitude of α_{mn} and γ_{mn}. The questions raised in this section are both answered affirmatively with the numerical quadrature and the analysis.

Table 9: $|\alpha_{mn}|$ estimated from E_θ and E_ϕ sampled on the sphere $a = 3\lambda$

	$n = 1$	$n = 2$	$n = 3$
$m = 0$	$8.14 \cdot 10^{-18}$	$2.81 \cdot 10^{-6}$	$2.22 \cdot 10^{-18}$
$m = 1$	1.00	$2.83 \cdot 10^{-17}$	$1.42 \cdot 10^{-6}$
$m = 2$		$4.74 \cdot 10^{-7}$	$3.55 \cdot 10^{-20}$
$m = 3$			$8.85 \cdot 10^{-9}$

Table 10: $|\gamma_{mn}|$ estimated from E_θ and E_ϕ sampled on the sphere $a = 3\lambda$

	$n = 1$	$n = 2$	$n = 3$
$m = 0$	$7.22 \cdot 10^{-20}$	$3.90 \cdot 10^{-20}$	$2.32 \cdot 10^{-20}$
$m = 1$	$1.38 \cdot 10^{-20}$	$4.91 \cdot 10^{-20}$	$7.17 \cdot 10^{-22}$
$m = 2$		$4.52 \cdot 10^{-22}$	$1.56 \cdot 10^{-20}$
$m = 3$			$7.43 \cdot 10^{-22}$

7 A Synthetic δ Field

Define a synthetic electric field with $\delta_{12} = 1$ as the only non-zero coefficient. The angular components of this electric field are

$$
\begin{aligned}
E_\theta(r, \theta, \phi) &= -j\omega\mu h_2^{(2)}(kr)\frac{P_2^1(\cos(\theta))}{\sin(\theta)}\cos(\phi) \\
E_\phi(r, \theta, \phi) &= j\omega\mu h_2^{(2)}(kr)\frac{dP_2^1(\cos(\theta))}{d\theta}\sin(\phi).
\end{aligned}
$$

For brevity, introduce

$$
E_0(r) := j\omega\mu h_2^{(2)}(kr) = j\omega\mu\exp(-jkr)\left\{-\frac{j}{kr} - \frac{3}{(kr)^2} + \frac{j3}{(kr)^3}\right\},
$$

using [3, Equation 11.150]. Use [3, Table 12.3 with footnote]

$$
P_2^1(\cos(\theta)) = -3\cos(\theta)\sin(\theta)
$$

to compute

$$
\frac{dP_2^1(\cos(\theta))}{d\theta} = 3 - 6\cos(\theta)^2.
$$

The electric fields are

$$
\begin{aligned}
E_\theta(r, \theta, \phi) &= 3E_0(r)\cos(\theta)\cos(\phi) \\
E_\phi(r, \theta, \phi) &= 3E_0(r)\{1 - 2\cos(\theta)^2\}\sin(\phi).
\end{aligned}
$$

38

Figure 26 reports the analysis and synthesis of this electric field at 300 MHz. The upper panels show $E_\theta(r, \theta, \phi)$ and $E_\phi(r, \theta, \phi)$ sampled on an angular grid at $r = 3$ m. The angular grid uses $N_\phi = 73$ and $N_\theta = 43$ sample points for an angular grid size of $\Delta\phi = 5°$ and $\Delta\theta = 4.3°$.
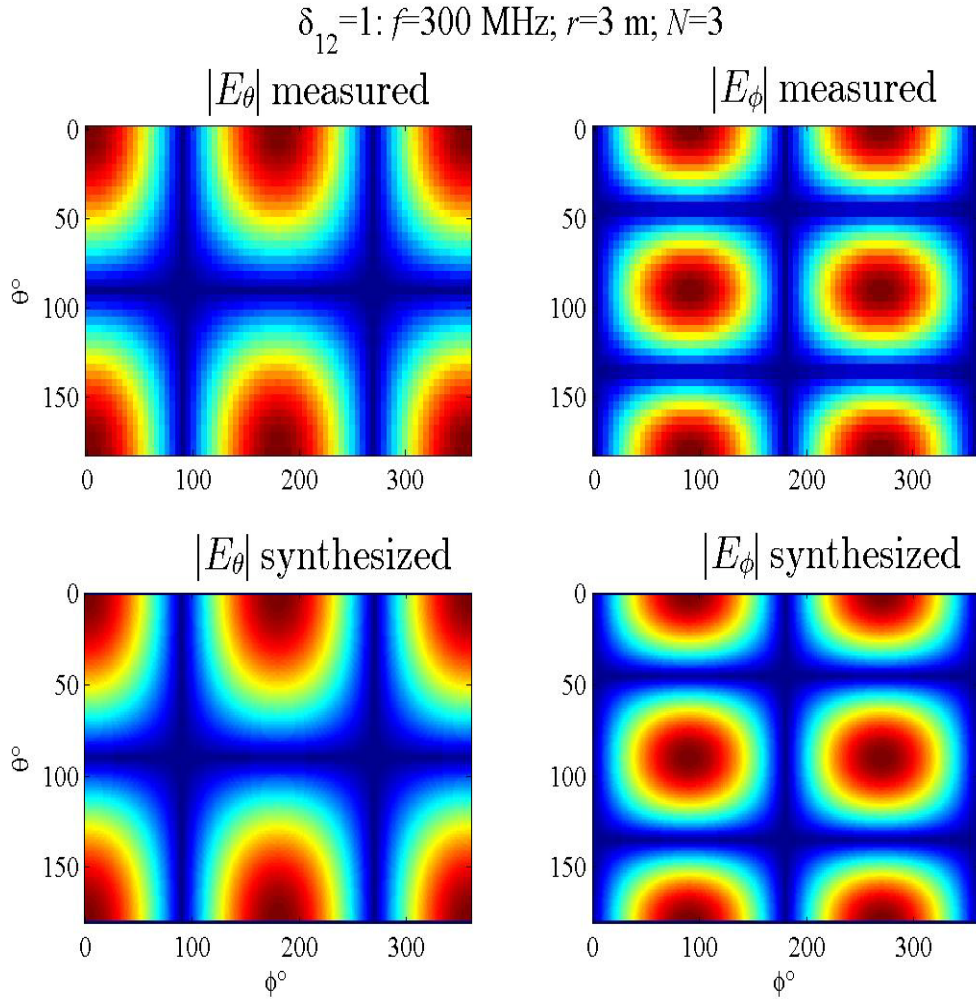
Figure 26: Synthesis of the $\delta_{12} = 1$ field.

The following tables report the magnitude of Sarkar's coefficients estimated from the sampled electric fields. All coefficients are smaller than 10^{-3} excepting $\delta_{12} \approx 1.02$.

Table 11: $|\alpha_{mn}|$ estimated from E_θ and E_ϕ sampled on the sphere $a = 3\lambda$ for the $\delta_{12} = 1$ antenna.

	$n = 1$	$n = 2$	$n = 3$
$m = 0$	$6.21 \cdot 10^{-15}$	$2.17 \cdot 10^{-5}$	$1.23 \cdot 10^{-14}$
$m = 1$	$2.68 \cdot 10^{-4}$	$7.81 \cdot 10^{-14}$	$3.62 \cdot 10^{-5}$
$m = 2$		$2.37 \cdot 10^{-6}$	$1.34 \cdot 10^{-16}$
$m = 3$			$2.83 \cdot 10^{-7}$

Table 12: $|\beta_{mn}|$ estimated from E_θ and E_ϕ sampled on the sphere $r = 3\lambda$ for the $\delta_{12} = 1$ antenna.

	$n = 1$	$n = 2$	$n = 3$
$m = 0$	0	0	0
$m = 1$	$4.16 \cdot 10^{-14}$	$2.25 \cdot 10^{-15}$	$8.02 \cdot 10^{-15}$
$m = 2$		$2.49 \cdot 10^{-15}$	$5.59 \cdot 10^{-16}$
$m = 3$			$4.97 \cdot 10^{-15}$

Table 13: $|\gamma_{mn}|$ estimated from E_θ and E_ϕ sampled on the sphere $r = 3\lambda$ for the $\delta_{12} = 1$ antenna.

	$n = 1$	$n = 2$	$n = 3$
$m = 0$	$3.85 \cdot 10^{-17}$	$2.49 \cdot 10^{-18}$	$3.61 \cdot 10^{-17}$
$m = 1$	$2.03 \cdot 10^{-17}$	$7.40 \cdot 10^{-18}$	$2.42 \cdot 10^{-18}$
$m = 2$		$7.97 \cdot 10^{-19}$	$5.15 \cdot 10^{-18}$
$m = 3$			$2.22 \cdot 10^{-19}$

Table 14: $|\delta_{mn}|$ estimated from E_θ and E_ϕ sampled on the sphere $r = 3\lambda$ for the $\delta_{12} = 1$ antenna.

	$n = 1$	$n = 2$	$n = 3$
$m = 0$	0	0	0
$m = 1$	$3.83 \cdot 10^{-16}$	$1.02 \cdot 10^{0}$	$1.22 \cdot 10^{-17}$
$m = 2$		$1.93 \cdot 10^{-18}$	$4.13 \cdot 10^{-9}$
$m = 3$			$3.29 \cdot 10^{-18}$

8 Horizontal Electric Dipole

Figure 27 shows an electric dipole of length $\Delta\ell$ centered at the origin and oriented along the x-axis.
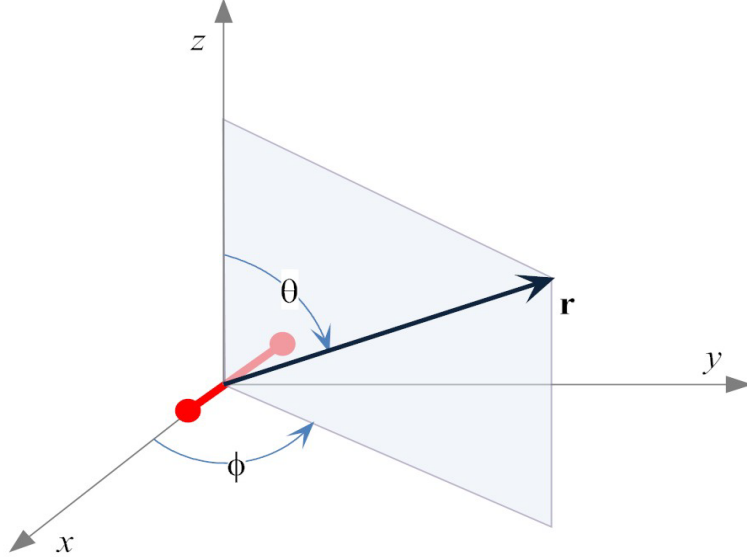
Figure 27: Horizontal Dipole.

If the dipole is carrying current i_A amps, the near field is

$$
E_\theta(r, \theta, \phi) = E_1(r) \cos(\theta) \left\{ \frac{1}{2} \sin(2\theta) \sin(\phi)^2 + \cos(\phi) \right\}
$$
$$
+ E_0(r) \sin(\theta) \cos(\theta)^2 \sin(\phi)^2 \tag{15}
$$
$$
E_\phi(r, \theta, \phi) = -E_1(r) \cos(\theta) \sin(\phi)(\cos(\theta) - \cos(\phi)\sin(\theta))
$$
$$
+ E_0(r) \sin(\theta) \sin(\phi)(\sin(\theta) + \cos(\phi)\cos(\theta)), \tag{16}
$$

where

$$
E_0(r) := \eta \frac{i_A \Delta\ell}{4\pi} k^2 \exp(-jkr) \left\{ \frac{j}{kr} + \frac{1}{(kr)^2} - \frac{j}{(kr)^3} \right\} \tag{17}
$$
$$
E_1(r) := \eta \frac{i_A \Delta\ell}{2\pi} k^2 \exp(-jkr) \left\{ \frac{1}{(kr)^2} - \frac{j}{(kr)^3} \right\}. \tag{18}
$$

8.1 Derivation

One way to obtain the near field of a horizontal dipole is to rotate the electric field of the Hertzian dipole. The Hertzian dipole has electric fields [7, Section 17.3]:

$$
\begin{aligned}
E_\theta(V; r, \theta, \phi) &= E_0(r)\sin(\theta) \\
E_\phi(V; r, \theta, \phi) &= 0 \\
E_r(V; r, \theta, \phi) &= E_1(r)\cos(\theta),
\end{aligned}
$$

where the "V" makes explicit that these fields reference the vertical dipole. The right-handed matrix R that rotates $\widehat{\mathbf{z}}$ into $\widehat{\mathbf{x}}$ while leaving $\widehat{\mathbf{y}}$ fixed is

$$
R = \begin{bmatrix} 0 & 0 & 1 \\ 0 & 1 & 0 \\ -1 & 0 & 0 \end{bmatrix}.
$$

If $\mathbf{E}(H; r, \theta, \phi)$ denotes the horizontal dipole field,

$$
\begin{aligned}
\mathbf{E}(H; r, \theta, \phi) &= R\mathbf{E}(V; r, \theta, \phi) \\
&= R\left\{ E_r(V; r, \theta, \phi)\widehat{\mathbf{r}} + E_\theta(V; r, \theta, \phi)\widehat{\boldsymbol{\theta}} \right\} \\
&= E_r(V; r, \theta, \phi)R\widehat{\mathbf{r}} + E_\theta(V; r, \theta, \phi)R\widehat{\boldsymbol{\theta}} \\
&= E_r(V; r, \theta, \phi)\left\{ \langle R\widehat{\mathbf{r}}, \widehat{\mathbf{r}}\rangle\widehat{\mathbf{r}} + \langle R\widehat{\mathbf{r}}, \widehat{\boldsymbol{\theta}}\rangle\widehat{\boldsymbol{\theta}} + \langle R\widehat{\mathbf{r}}, \widehat{\boldsymbol{\phi}}\rangle\widehat{\boldsymbol{\phi}} \right\} \\
&\quad + E_\theta(V; r, \theta, \phi)\left\{ \langle R\widehat{\boldsymbol{\theta}}, \widehat{\mathbf{r}}\rangle\widehat{\mathbf{r}} + \langle R\widehat{\boldsymbol{\theta}}, \widehat{\boldsymbol{\theta}}\rangle\widehat{\boldsymbol{\theta}} + \langle R\widehat{\boldsymbol{\theta}}, \widehat{\boldsymbol{\phi}}\rangle\widehat{\boldsymbol{\phi}} \right\} \\
&= \widehat{\mathbf{r}}\left\{ E_r(V; r, \theta, \phi)\langle R\widehat{\mathbf{r}}, \widehat{\mathbf{r}}\rangle + E_\theta(V; r, \theta, \phi)\langle R\widehat{\boldsymbol{\theta}}, \widehat{\mathbf{r}}\rangle \right\} \\
&\quad + \widehat{\boldsymbol{\theta}}\left\{ E_r(V; r, \theta, \phi)\langle R\widehat{\mathbf{r}}, \widehat{\boldsymbol{\theta}}\rangle + E_\theta(V; r, \theta, \phi)\langle R\widehat{\boldsymbol{\theta}}, \widehat{\boldsymbol{\theta}}\rangle \right\} \\
&\quad + \widehat{\boldsymbol{\phi}}\left\{ E_r(V; r, \theta, \phi)\langle R\widehat{\mathbf{r}}, \widehat{\boldsymbol{\phi}}\rangle + E_\theta(V; r, \theta, \phi)\langle R\widehat{\boldsymbol{\theta}}, \widehat{\boldsymbol{\phi}}\rangle \right\}.
\end{aligned}
$$

The action of the rotation matrix R on the radial vector

$$
\begin{aligned}
R\widehat{\mathbf{r}} &= \begin{bmatrix} 0 & 0 & 1 \\ 0 & 1 & 0 \\ -1 & 0 & 0 \end{bmatrix} \begin{bmatrix} \sin(\theta)\cos(\phi) \\ \sin(\theta)\sin(\phi) \\ \cos(\theta) \end{bmatrix} \\
&= \begin{bmatrix} \cos(\theta) \\ \sin(\theta)\sin(\phi) \\ -\sin(\theta)\cos(\phi) \end{bmatrix} \\
&= \langle R\widehat{\mathbf{r}}, \widehat{\mathbf{r}}\rangle\widehat{\mathbf{r}} + \langle R\widehat{\mathbf{r}}, \widehat{\boldsymbol{\theta}}\rangle\widehat{\boldsymbol{\theta}} + \langle R\widehat{\mathbf{r}}, \widehat{\boldsymbol{\phi}}\rangle\widehat{\boldsymbol{\phi}}
\end{aligned}
$$

42

has coefficients

$$\langle R\widehat{\mathbf{r}}, \widehat{\mathbf{r}} \rangle = \sin(\theta)^2 \sin(\phi)^2$$

$$\langle R\widehat{\mathbf{r}}, \widehat{\boldsymbol{\theta}} \rangle = \frac{1}{2}\sin(2\theta)\sin(\phi)^2 + \cos(\phi)$$

$$\langle R\widehat{\mathbf{r}}, \widehat{\boldsymbol{\phi}} \rangle = -\sin(\phi)(\cos(\theta) - \cos(\phi)\sin(\theta)).$$

The action of the rotation matrix R on the elevation vector

$$
R\widehat{\boldsymbol{\theta}} = \begin{bmatrix} 0 & 0 & 1 \\ 0 & 1 & 0 \\ -1 & 0 & 0 \end{bmatrix} \begin{bmatrix} \cos(\theta)\cos(\phi) \\ \cos(\theta)\sin(\phi) \\ -\sin(\theta) \end{bmatrix}
$$

$$
= \begin{bmatrix} -\sin(\theta) \\ \cos(\theta)\sin(\phi) \\ -\cos(\theta)\cos(\phi) \end{bmatrix}
$$

$$
= \langle R\widehat{\boldsymbol{\theta}}, \widehat{\mathbf{r}} \rangle\widehat{\mathbf{r}} + \langle R\widehat{\boldsymbol{\theta}}, \widehat{\boldsymbol{\theta}} \rangle\widehat{\boldsymbol{\theta}} + \langle R\widehat{\boldsymbol{\theta}}, \widehat{\boldsymbol{\phi}} \rangle\widehat{\boldsymbol{\phi}}
$$

has coefficients

$$\langle R\widehat{\boldsymbol{\theta}}, \widehat{\mathbf{r}} \rangle = \frac{1}{2}\sin(2\theta)\sin(\phi)^2 - \cos(\phi)$$

$$\langle R\widehat{\boldsymbol{\theta}}, \widehat{\boldsymbol{\theta}} \rangle = \cos(\theta)^2 \sin(\phi)^2$$

$$\langle R\widehat{\boldsymbol{\theta}}, \widehat{\boldsymbol{\phi}} \rangle = \sin(\phi)(\sin(\theta) + \cos(\phi)\cos(\theta)).$$

The elevation component of the horizonal dipole is

$$
\begin{aligned}
E_\theta(H; r, \theta, \phi) &= E_r(V; r, \theta, \phi)\langle R\widehat{\mathbf{r}}, \widehat{\boldsymbol{\theta}} \rangle + E_\theta(V; r, \theta, \phi)\langle R\widehat{\boldsymbol{\theta}}, \widehat{\boldsymbol{\theta}} \rangle \\
&= E_r(V; r, \theta, \phi)\left\{ \frac{1}{2}\sin(2\theta)\sin(\phi)^2 + \cos(\phi) \right\} \\
&\quad + E_\theta(V; r, \theta, \phi)\cos(\theta)^2 \sin(\phi)^2 \\
&= E_1(r)\cos(\theta)\left\{ \frac{1}{2}\sin(2\theta)\sin(\phi)^2 + \cos(\phi) \right\} \\
&\quad + E_0(r)\sin(\theta)\cos(\theta)^2 \sin(\phi)^2.
\end{aligned}
$$

The azimuth component of the horizonal dipole is

$$
\begin{aligned}
E_\phi(H; r, \theta, \phi) &= E_r(V; r, \theta, \phi)\langle R\widehat{\mathbf{r}}, \widehat{\boldsymbol{\phi}} \rangle + E_\theta(V; r, \theta, \phi)\langle R\widehat{\boldsymbol{\theta}}, \widehat{\boldsymbol{\phi}} \rangle \\
&= -E_r(V; r, \theta, \phi)\sin(\phi)(\cos(\theta) - \cos(\phi)\sin(\theta)) \\
&\quad + E_\theta(V; r, \theta, \phi)\sin(\phi)(\sin(\theta) + \cos(\phi)\cos(\theta)) \\
&= -E_1(r)\cos(\theta)\sin(\phi)(\cos(\theta) - \cos(\phi)\sin(\theta)) \\
&\quad + E_0(r)\sin(\theta)\sin(\phi)(\sin(\theta) + \cos(\phi)\cos(\theta)).
\end{aligned}
$$

8.2 Analysis

This section verifies that the β_{mn}'s and the γ_{mn}'s of Sarkar's expansion vanish. The β_{mn}'s vanish because of the orthogonality between $\cos(\phi)$ and $\sin(\phi)$ and the basis functions $\sin(m\phi)$ and $\cos(m\phi)$, respectively,

$$\beta_{mn} = \frac{a}{kah_n^{(2)\prime}(ka) + h_n^{(2)}(ka)} \frac{(2n+1)(n-m)!}{2n(n+1)(n+m)!} \frac{\epsilon_m}{2\pi} \{b_{\phi;mn} + b_{\theta;mn}\}.$$

Integrating each term separately,

$$
\begin{aligned}
b_{\phi;mn} &= \int_0^{2\pi} d\phi \int_0^\pi d\theta \, m E_\phi(a,\theta,\phi) P_n^m(\cos(\theta)) \cos(m\phi) \\
&= \int_0^{2\pi} d\phi \int_0^\pi d\theta \, m\{-E_1(r)\cos(\theta)\sin(\phi)(\cos(\theta)-\cos(\phi)\sin(\theta)) \\
&\quad + E_0(r)\sin(\theta)\sin(\phi)(\sin(\theta)+\cos(\phi)\cos(\theta))\} P_n^m(\cos(\theta))\cos(m\phi) \\
&= -mE_1(a)\int_0^{2\pi}\sin(\phi)\cos(m\phi)d\phi \int_0^\pi \cos(\theta)^2 P_n^m(\cos(\theta))d\theta \\
&\quad + mE_1(a)\int_0^{2\pi}\sin(\phi)\cos(\phi)\cos(m\phi)d\phi \int_0^\pi \cos(\theta)\sin(\theta)P_n^m(\cos(\theta))d\theta \\
&\quad + mE_0(a)\int_0^{2\pi}\sin(\phi)\cos(m\phi)d\phi \int_0^\pi \sin(\theta)^2 P_n^m(\cos(\theta))d\theta \\
&\quad + mE_0(a)\int_0^{2\pi}\sin(\phi)\cos(\phi)\cos(m\phi)d\phi \int_0^\pi \sin(\theta)\cos(\theta)P_n^m(\cos(\theta))d\theta \\
&= 0
\end{aligned}
$$

because the $\cos(m\phi)$'s are even functions while $\sin(\phi)$ and $\sin(\phi)\cos(\phi)$ are odd functions.

$$
\begin{aligned}
b_{\theta;mn} &= \int_0^{2\pi} d\phi \int_0^\pi d\theta \, E_\theta(a,\theta,\phi)\frac{dP_n^m(\cos(\theta))}{d\theta}\sin(\theta)\sin(m\phi) \\
&= -E_0(a)\int_0^{2\pi}\cos(\phi)\sin(m\phi)d\phi \int_0^\pi \cos(\theta)\sin(\theta)\frac{dP_n^m(\cos(\theta))}{d\theta}d\theta \\
&= -E_0(a)\int_0^{2\pi}\cos(\phi)\sin(m\phi)d\phi \int_0^\pi \sin(\theta)\cos(\theta)\frac{dP_n^m(\cos(\theta))}{d\theta}d\theta \\
&= 0.
\end{aligned}
$$

Thus, the β_{mn}'s must vanish in a credible quadrature (see Table 16).

The γ_{mn}'s vanish because of the orthogonality between $\cos(\phi)$ and $\sin(\phi)$ and the basis functions $\sin(m\phi)$ and $\cos(m\phi)$, respectively.

$$\gamma_{mn} = \frac{1}{j\omega\mu h_n^{(2)}(ka)} \frac{(2n+1)(n-m)!}{2n(n+1)(n+m)!}\{c_{\phi;mn} + c_{\theta;mn}\}.$$

Integrating each term separately,

$$c_{\phi;mn} := \int_0^{2\pi} d\phi \int_0^\pi d\theta \; E_\phi(a,\theta,\phi)\frac{dP_n^m(\cos(\theta))}{d\theta}\sin(\theta)\cos(m\phi)$$

$$= \int_0^{2\pi} d\phi \int_0^\pi d\theta \; \{-E_1(a)\cos(\theta)\sin(\phi)(\cos(\theta)-\cos(\phi)\sin(\theta))$$

$$+E_0(a)\sin(\theta)\sin(\phi)(\sin(\theta)+\cos(\phi)\cos(\theta))\}\frac{dP_n^m(\cos(\theta))}{d\theta}\sin(\theta)\cos(m\phi)$$

$$= -E_1(a)\int_0^{2\pi}\sin(\phi)\cos(m\phi)d\phi\int_0^\pi\sin(\theta)\cos(\theta)^2\frac{dP_n^m(\cos(\theta))}{d\theta}d\theta$$

$$+E_1(a)\int_0^{2\pi}\sin(\phi)\cos(\phi)\cos(m\phi)d\phi\int_0^\pi\cos(\theta)\sin(\theta)^2\frac{dP_n^m(\cos(\theta))}{d\theta}d\theta$$

$$+E_0(a)\int_0^{2\pi}\sin(\phi)\cos(m\phi)d\phi\int_0^\pi\sin(\theta)^3\frac{dP_n^m(\cos(\theta))}{d\theta}d\theta$$

$$+E_0(a)\int_0^{2\pi}\sin(\phi)\cos(\phi)\cos(m\phi)d\phi\int_0^\pi\sin(\theta)^2\cos(\theta)\frac{dP_n^m(\cos(\theta))}{d\theta}d\theta$$

$$= 0$$

because the $\cos(m\phi)$'s are even functions while $\sin(\phi)$ and $\sin(\phi)\cos(\phi)$ are odd functions.

$$c_{\theta;mn} := \int_0^{2\pi} d\phi \int_0^\pi d\theta \; mE_\theta(a,\theta,\phi)P_n^m(\cos(\theta))\sin(m\phi)$$

$$= \int_0^{2\pi} d\phi \int_0^\pi d\theta \; m\{E_1(a)\cos(\theta)\{\sin(2\theta)\sin(\phi)^2/2+\cos(\phi)\}$$

$$+E_0(a)\sin(\theta)\cos(\theta)^2\sin(\phi)^2\}P_n^m(\cos(\theta))\sin(m\phi)$$

$$= \frac{m}{2}E_1(a)\int_0^{2\pi}\sin(\phi)^2\sin(m\phi)d\phi\int_0^\pi\cos(\theta)\sin(2\theta)P_n^m(\cos(\theta))d\theta$$

$$+mE_1(a)\int_0^{2\pi}\cos(\phi)\sin(m\phi)d\phi\int_0^\pi\cos(\theta)P_n^m(\cos(\theta))d\theta$$

$$+mE_0(a)\int_0^{2\pi}\sin(\phi)^2\sin(m\phi)d\phi\int_0^\pi\sin(\theta)\cos(\theta)^2P_n^m(\cos(\theta))d\theta$$

$$= 0$$

because the $\sin(m\phi)$'s are odd functions while $\cos(\phi)$ are $\sin(\phi)^2$ are even functions over $[0, 2\pi]$. Thus, the γ_{mn}'s must vanish in a credible quadrature (see Table 17).

45

Table 15: $|\alpha_{mn}|$ estimated from E_θ and E_ϕ sampled on the sphere $a = 3\lambda$ for the Horizontal Dipole.

	$n=1$	$n=2$	$n=3$	$n=4$	$n=5$
$m=0$	1.90	$5.31 \cdot 10^{-6}$	1.27	$1.21 \cdot 10^{-6}$	$1.28 \cdot 10^{-8}$
$m=1$	9.48	$5.01 \cdot 10^{-7}$	$1.41 \cdot 10^{-6}$	$2.48 \cdot 10^{-6}$	$1.88 \cdot 10^{-7}$
$m=2$		$1.03 \cdot 10^{-7}$	0.212	$6.82 \cdot 10^{-9}$	$9.84 \cdot 10^{-8}$
$m=3$			$1.19 \cdot 10^{-8}$	$7.48 \cdot 10^{-8}$	$4.32 \cdot 10^{-10}$
$m=4$				$1.32 \cdot 10^{-9}$	$8.51 \cdot 10^{-9}$
$m=5$					$1.36 \cdot 10^{-10}$

Table 16: $|\beta_{mn}|$ estimated from E_θ and E_ϕ sampled on the sphere $r = 3\lambda$ for the Horizontal Dipole.

	$n=1$	$n=2$	$n=3$	$n=4$	$n=5$
$m=0$	0	0	0	0	0
$m=1$	$8.31 \cdot 10^{-16}$	$4.46 \cdot 10^{-17}$	$3.61 \cdot 10^{-17}$	$7.05 \cdot 10^{-18}$	$5.58 \cdot 10^{-18}$
$m=2$		$1.74 \cdot 10^{-16}$	$3.12 \cdot 10^{-17}$	$3.14 \cdot 10^{-18}$	$1.40 \cdot 10^{-17}$
$m=3$			$6.61 \cdot 10^{-17}$	$9.67 \cdot 10^{-18}$	$1.58 \cdot 10^{-18}$
$m=4$				$3.33 \cdot 10^{-17}$	$2.79 \cdot 10^{-19}$
$m=5$					$3.44 \cdot 10^{-18}$

Table 17: $|\gamma_{mn}|$ estimated from E_θ and E_ϕ sampled on the sphere $r = 3\lambda$ for the Horizontal Dipole.

	$n=1$	$n=2$	$n=3$	$n=4$	$n=5$
$m=0$	$1.36 \cdot 10^{-19}$	$1.35 \cdot 10^{-19}$	$1.53 \cdot 10^{-19}$	$7.26 \cdot 10^{-19}$	$1.68 \cdot 10^{-19}$
$m=1$	$9.59 \cdot 10^{-19}$	$1.07 \cdot 10^{-18}$	$2.02 \cdot 10^{-19}$	$8.53 \cdot 10^{-21}$	$2.78 \cdot 10^{-20}$
$m=2$		$3.85 \cdot 10^{-20}$	$8.87 \cdot 10^{-20}$	$6.03 \cdot 10^{-20}$	$2.41 \cdot 10^{-20}$
$m=3$			$1.89 \cdot 10^{-21}$	$2.42 \cdot 10^{-20}$	$1.20 \cdot 10^{-20}$
$m=4$				$7.81 \cdot 10^{-21}$	$6.08 \cdot 10^{-21}$
$m=5$					$1.56 \cdot 10^{-21}$

Table 18: $|\delta_{mn}|$ estimated from E_θ and E_ϕ sampled on the sphere $r = 3\lambda$ for the Horizontal Dipole.

	$n = 1$	$n = 2$	$n = 3$	$n = 4$	$n = 5$
$m = 0$	0	0	0		0
$m = 1$	$6.08 \cdot 10^{-8}$	$8.33 \cdot 10^{-3}$	$7.16 \cdot 10^{-9}$	$2.06 \cdot 10^{-9}$	$1.04 \cdot 10^{-9}$
$m = 2$		$1.39 \cdot 10^{-3}$	$1.47 \cdot 10^{-10}$	$7.13 \cdot 10^{-10}$	$2.52 \cdot 10^{-11}$
$m = 3$			$1.27 \cdot 10^{-9}$	$1.80 \cdot 10^{-11}$	$2.24 \cdot 10^{-10}$
$m = 4$				$1.30 \cdot 10^{-10}$	$1.79 \cdot 10^{-12}$
$m = 5$					$1.08 \cdot 10^{-11}$

8.3 Synthesis

The following figures show the synthesis for this antenna. The electric fields are sampled on an angular grid at a radial distance of 3 m. This angular grid is determined by sampling $N_\phi = 73$ and $N_\theta = 43$ for a angular grid size of $\Delta\phi = 5°$ and $\Delta\theta = 4.3°$. Figure 28 is a 3-D view of the magnitude of the electric fields. The upper panels show $E_\theta(r,\theta,\phi)$ and $E_\phi(r,\theta,\phi)$ sampled on an angular grid. The lower panels show the corresponding synthesis. Figure 29 displays the same information in two-dimensional images.

Horizontal Dipole: f=300 MHz; r=3 m
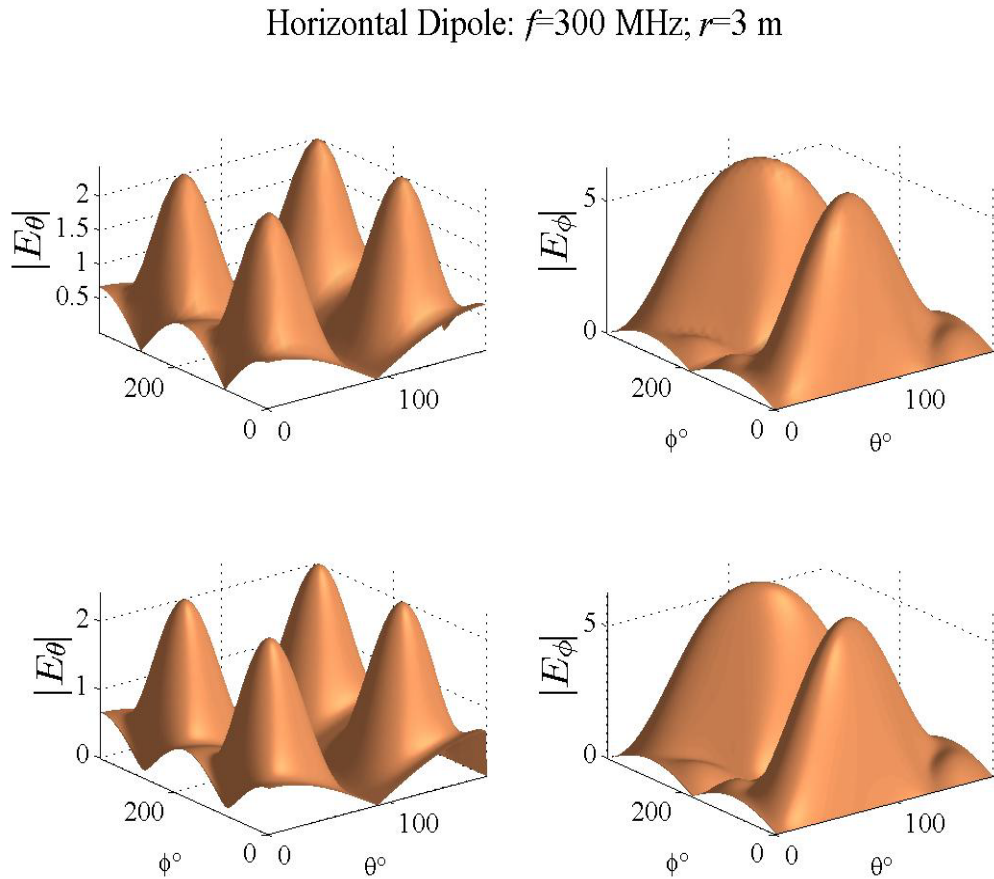
Figure 28: Horizontal dipole at 300 MHz in 3-D; $i_A = 1$ amp, $\ell = \lambda/10$; upper panels are the simulated fields, lower panels are the synthesized fields.

48
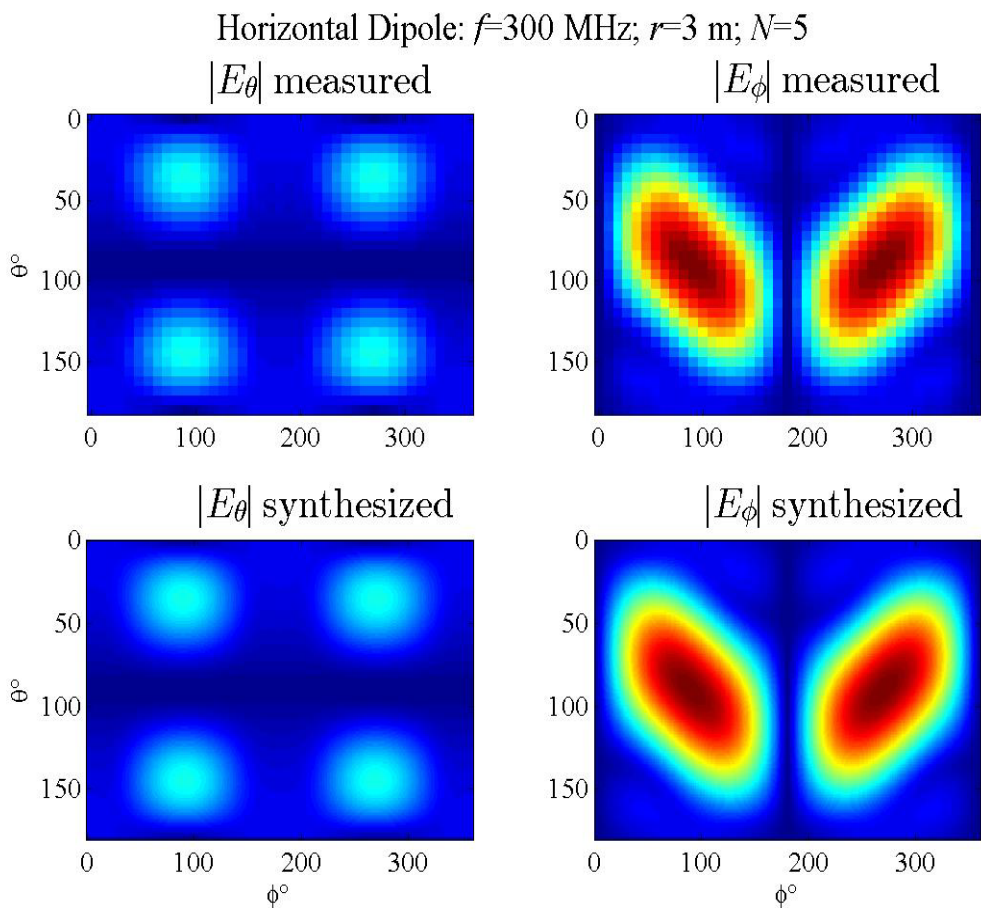
Figure 29: Horizontal dipole images at 300 MHz; $i_A = 1$ amp, $\ell = \lambda/10$; upper panels are the simulated fields, lower panels are the synthesized fields.

8.4   Far Field

From Equations 17 and 18, the radial terms behave like

$$
\begin{aligned}
E_0(r) &= \eta \frac{i_A \Delta \ell}{4\pi} k \exp(-jkr)\frac{j}{r} + \mathcal{O}[r^{-2}] \\
E_1(r) &= \mathcal{O}[r^{-2}].
\end{aligned}
$$

Substitution into Equations 15 and 16 gives the behavior of the electric field:

$$
\begin{aligned}
E_\theta(r, \theta, \phi) &= E_0(r) \sin(\theta) \cos(\theta)^2 \sin(\phi)^2 + \mathcal{O}[r^{-2}] \\
E_\phi(r, \theta, \phi) &= E_0(r) \sin(\theta) \sin(\phi)(\sin(\theta) + \cos(\phi) \cos(\theta)) + \mathcal{O}[r^{-2}].
\end{aligned}
$$

The magnitude squared of the far field has the expansion

$$
\begin{aligned}
\|\mathbf{E}(r, \theta, \phi)\|^2 &= |E_\theta(r, \theta, \phi)|^2 + |E_\phi(r, \theta, \phi)|^2 + |E_r(r, \theta, \phi)|^2 \\
&= |E_0(r)|^2 \sin(\theta)^2 \cos(\theta)^4 \sin(\phi)^4 \\
&\quad + |E_0(r)|^2 \sin(\theta)^2 \sin(\phi)^2 (\sin(\theta) + \cos(\phi) \cos(\theta))^2 + \mathcal{O}[(kr)^{-3}] \\
&= |E_0(r)|^2 \sin(\theta)^2 \sin(\phi)^2 \left\{ \cos(\theta)^4 \sin(\phi)^2 + (\sin(\theta) + \cos(\phi) \cos(\theta))^2 \right\} \\
&\quad + \mathcal{O}[(kr)^{-3}].
\end{aligned}
$$

The pattern function of the electric field is

$$
\begin{aligned}
F(\theta, \phi) &= \lim_{r \to \infty} r \|\mathbf{E}(r, \theta, \phi)\| \\
&= \lim_{r \to \infty} r |E_0(r)| \sin(\theta) |\sin(\phi)| \\
&\quad \times \sqrt{\cos(\theta)^4 \sin(\phi)^2 + (\sin(\theta) + \cos(\phi) \cos(\theta))^2} \\
&= \eta \frac{|i_A| \Delta \ell k}{4\pi} \sin(\theta) |\sin(\phi)| \\
&\quad \times \sqrt{\cos(\theta)^4 \sin(\phi)^2 + (\sin(\theta) + \cos(\phi) \cos(\theta))^2}.
\end{aligned}
$$

Figure 30 plots this far-field pattern. Figure 31 is the approximation to the pattern

$$
F(\theta, \phi) \approx r \sqrt{|E_\theta(r, \theta, \phi)|^2 + |E_\phi(r, \theta, \phi)|^2}.
$$

at $r = 100$ m. Figure 32 plots the corresponding approximation to the pattern function using the electric field synthesized by Sarkar's coefficients. The pattern functions are comparable in all three figures.
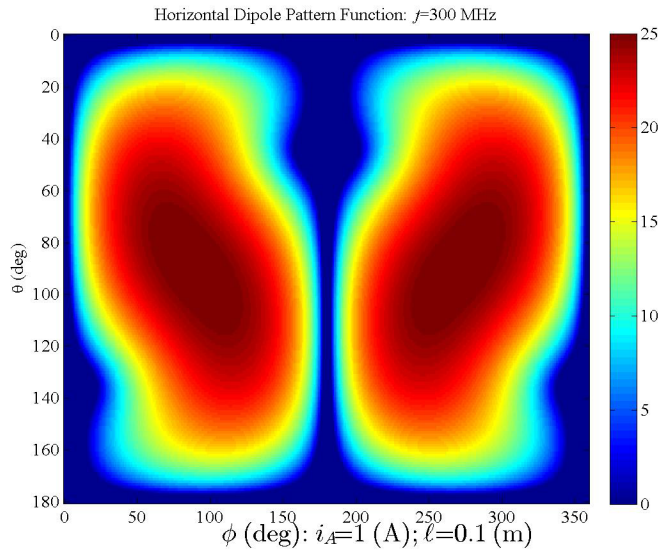
Figure 30: Pattern function for the horizontal dipole: $i_A = 1$ amp, $\ell = \lambda/10$ m.
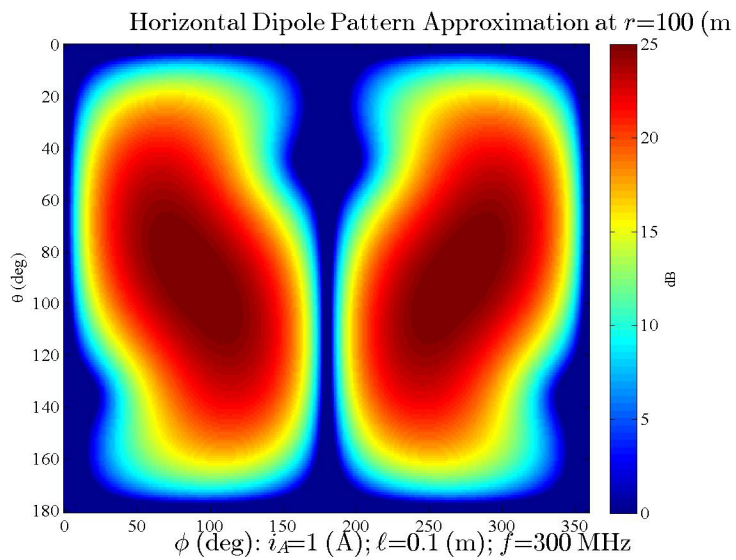
Figure 31: Pattern function approximation at $r = 100$ m.
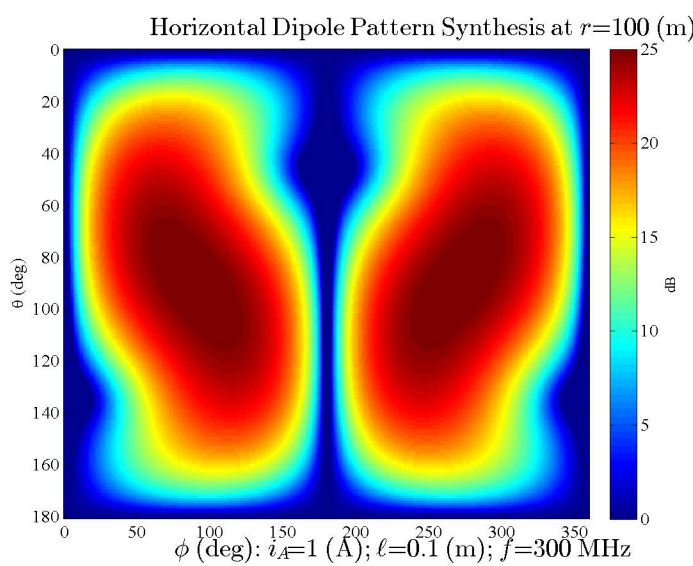
Figure 32: Synthetic pattern function approximation at $r = 100$ m.

9 Tilted Dipole

Figure 33 is a schematic of a tilted dipole raised over an infinite ground plane.
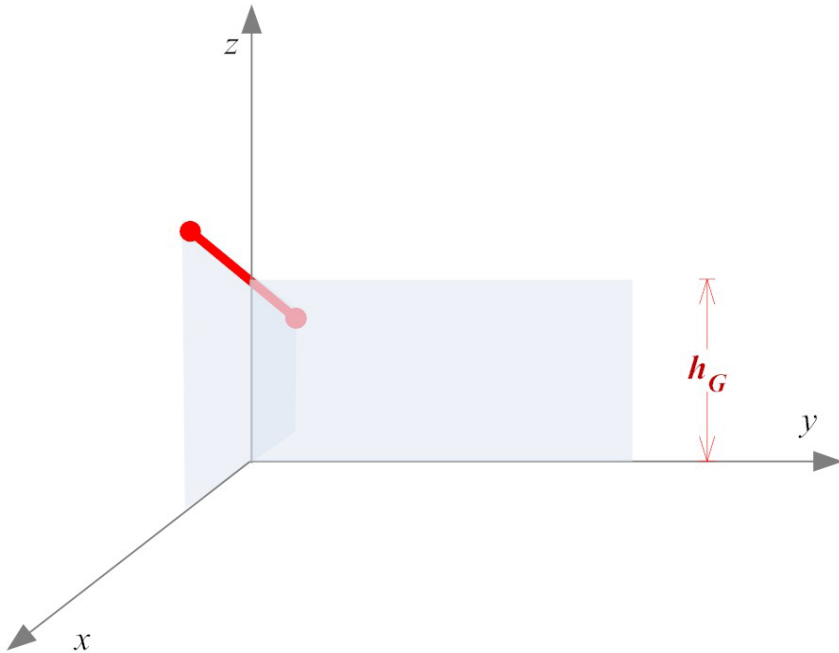
Figure 33: Dipole tilted in the $x \times z$-plane and lifted over a perfect ground.

This dipole is simulated in Mini-NEC with the following specifications:

- Length $\ell = 8$ ft

- Tilted from vertical in the $x \times z$-plane by $\theta_T = 45°$

- Lifted over the ground by $h_G = 6$ ft

Table 19 lists the Mini-NEC description for completeness, where the dipole is driven at 29 MHz. Figure 34 reports the resulting electric fields measured on a hemisphere with a radius of 80 ft or 24 m.

```
D:\antenna\NearToFarField\TiltedDipole\TiltedDipole01_80  01-22-2013   09:51:19


Tilted Dipole
45 degrees elevation in the x-z plane
8 long
6 ft above the ground


GEOMETRY
Dimensions in feet
Environment: perfect ground

wire  caps X              Y              Z            radius      segs
 1    none 2.8284         0              8.8284       .001        11
           -2.8284        0              3.1716


Number of wires        =  1
        current nodes  =  10


                        minimum              maximum
Individual wires      wire    value        wire   value
segment length         1     .727266        1     .727266
segment/radius ratio   1     727.266        1     727.266
radius                 1     1.E-03         1     1.E-03


ELECTRICAL DESCRIPTION
Frequencies (MHz)
     frequency                no. of  segment length (wavelengths)
 no. lowest       step        steps   minimum       maximum
 1   29.          0           1       .0214425      .0214425

Sources
source node    sector  magnitude     phase        type
 1      5       1       1.            0            voltage
```
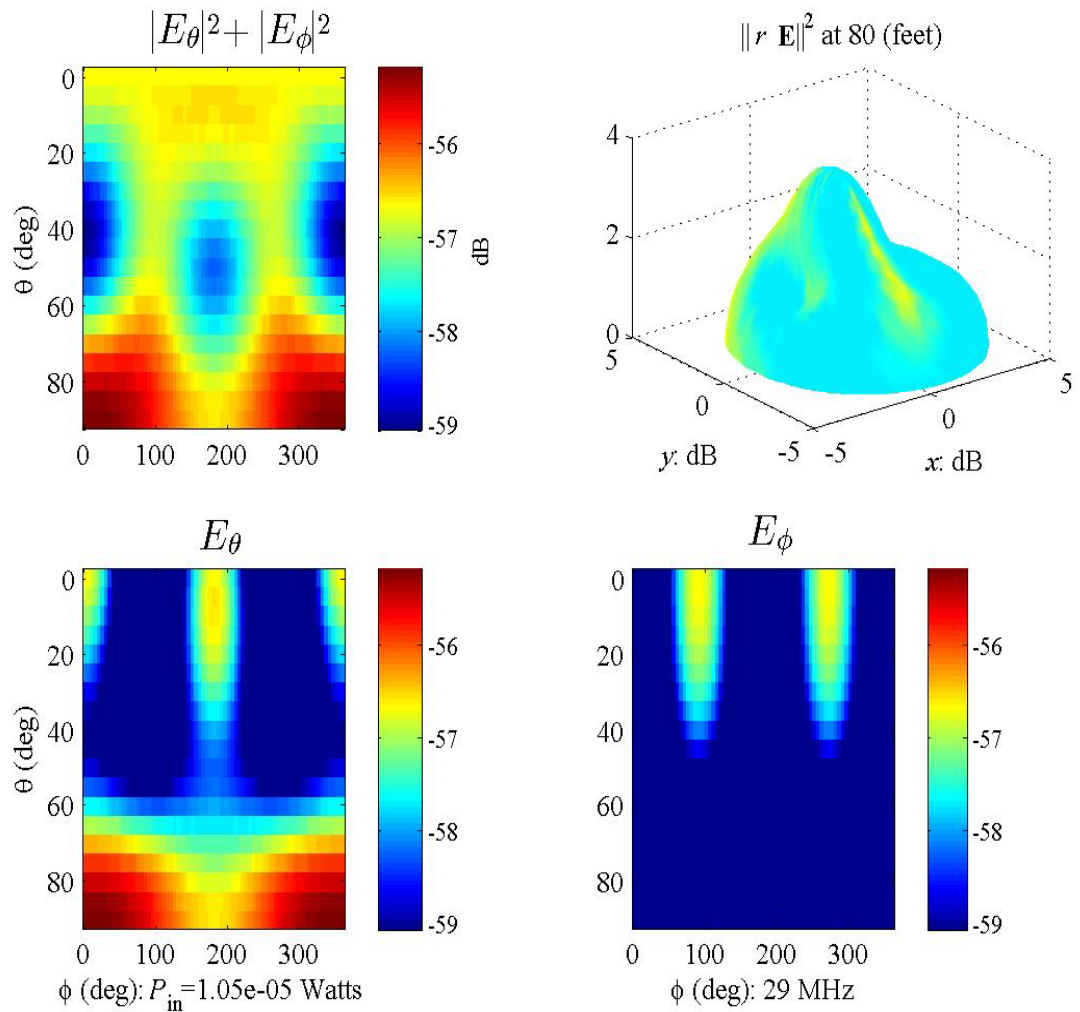
Figure 34: MiniNEC simulation of the tilted dipole at 29 MHz; electric fields are measured at 80 ft.

9.1 Synthesis

Synthesis requires extending the electric fields from the upper hemisphere to the entire sphere. If $E_\theta^+(\theta, \phi)$ and $E_\phi^+(\theta, \phi)$ denote the simulated electric fields on the upper hemisphere, make the even extension

$$E_\theta(\theta, \phi) = \begin{cases} E_\theta^+(\theta, \phi) & 0 \leq \theta \leq \pi/2 \\ E_\theta^+(\pi - \theta, \phi) & \pi/2 \leq \theta \leq \pi \end{cases}$$

and the odd extension

$$E_\phi(\theta, \phi) = \begin{cases} E_\phi^+(\theta, \phi) & 0 \leq \theta \leq \pi/2 \\ -E_\phi^+(\pi - \theta, \phi) & \pi/2 \leq \theta \leq \pi \end{cases} .$$

Figures 35 and 36 report the magnitude of the sampled fields. The mesh plot is used to emphasize that fields are sampled on the upper hemisphere with $N_\phi = 73$ samples in $0 \leq \phi \leq 360°$ using the azimuth increment $\Delta\phi = 5°$ and $N_\theta = 19$ samples in $0 \leq \phi \leq 90°$ using the zenith increment $\Delta\theta = 5°$. Figure 36 verifies that E_ϕ vanishes at the ground plane.
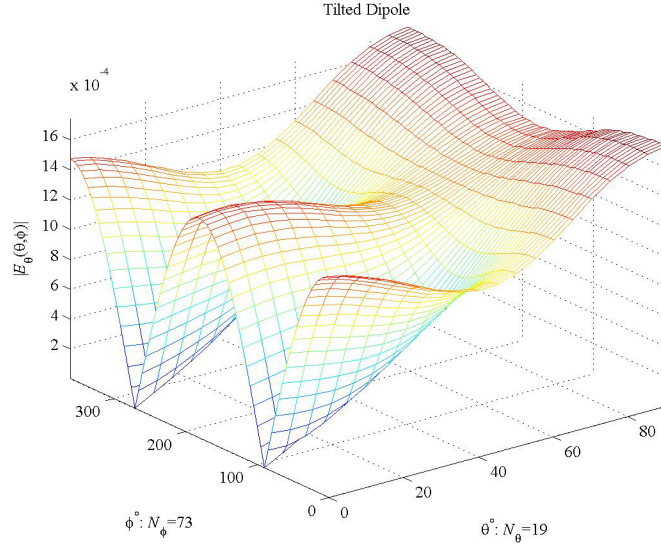
Figure 35: MiniNEC simulation of the tilted dipole at 29 MHz; electric fields are measured at 80 ft.

Tables 20, 21, 22, and 23 report the coefficients estimated from the sampled fields. The relatively small size of γ_{mn} suggests that these coefficients are zero. Likewise, the β_{mn} and δ_{mn} are relatively small with respect to α_{mn}. Consequently, when the synthesis undertaken, the α terms will dominate.

56
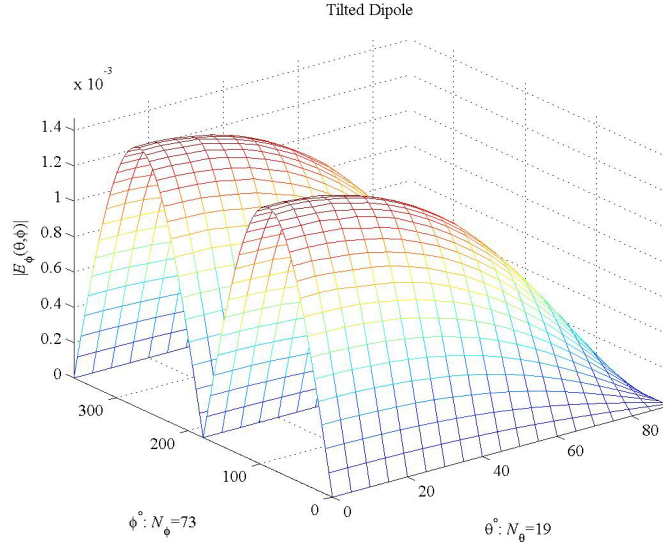
Figure 36: MiniNEC simulation of the tilted dipole at 29 MHz; electric fields are measured at 80 ft.

Table 20: $|\alpha_{mn}|$ estimated from E_θ and E_ϕ sampled on the sphere at 80 ft for the tilted dipole.

	$n = 1$	$n = 2$	$n = 3$
$m = 0$	$3.63 \cdot 10^{-2}$	$1.09 \cdot 10^{-3}$	$2.72 \cdot 10^{-3}$
$m = 1$	$9.48 \cdot 10^{-4}$	$6.35 \cdot 10^{-3}$	$1.05 \cdot 10^{-4}$
$m = 2$		$5.91 \cdot 10^{-6}$	$3.30 \cdot 10^{-5}$
$m = 3$			$8.49 \cdot 10^{-7}$

Table 21: $|\beta_{mn}|$ estimated from E_θ and E_ϕ sampled on the sphere at 80 ft for the tilted dipole.

	$n = 1$	$n = 2$	$n = 3$
$m = 0$	0	0	0
$m = 1$	$1.32 \cdot 10^{-6}$	$1.95 \cdot 10^{-7}$	$5.98 \cdot 10^{-7}$
$m = 2$		$1.34 \cdot 10^{-7}$	$4.23 \cdot 10^{-8}$
$m = 3$			$4.31 \cdot 10^{-8}$

57

Table 22: $|\gamma_{mn}|$ estimated from E_θ and E_ϕ sampled on the sphere at 80 ft for the tilted dipole.

	$n = 1$	$n = 2$	$n = 3$
$m = 0$	$4.04 \cdot 10^{-11}$	$4.06 \cdot 10^{-11}$	$1.80 \cdot 10^{-11}$
$m = 1$	$5.80 \cdot 10^{-9}$	$1.93 \cdot 10^{-9}$	$6.25 \cdot 10^{-10}$
$m = 2$		$4.00 \cdot 10^{-10}$	$1.65 \cdot 10^{-10}$
$m = 3$			$5.45 \cdot 10^{-11}$

Table 23: $|\delta_{mn}|$ estimated from E_θ and E_ϕ sampled on the sphere at 80 ft for the tilted dipole.

	$n = 1$	$n = 2$	$n = 3$
$m = 0$	0	0	0
$m = 1$	$4.95 \cdot 10^{-5}$	$6.20 \cdot 10^{-7}$	$6.46 \cdot 10^{-7}$
$m = 2$		$3.04 \cdot 10^{-9}$	$3.92 \cdot 10^{-9}$
$m = 3$			$2.43 \cdot 10^{-9}$

Figure 37 compares the sampled and synthesized fields at 29 MHz on a upper hemisphere with an 80-ft radius. The upper panels are the sampled fields computed from MiniNEC. The lower panels are the synthesized fields computed from Sarkar's expansion with only $N = 3$ terms and the coefficients α_{mn}, β_{mn}, γ_{mn}, δ_{mn}, estimated from the sampled fields in Figures 35 and 36. These images use the same linear color scale with the magnitude of the fields plotted in V/m. Comparison between the sampled fields from MiniNEC and the synthesized field of Sarkar shows that differences in the magnitudes are relatively small.
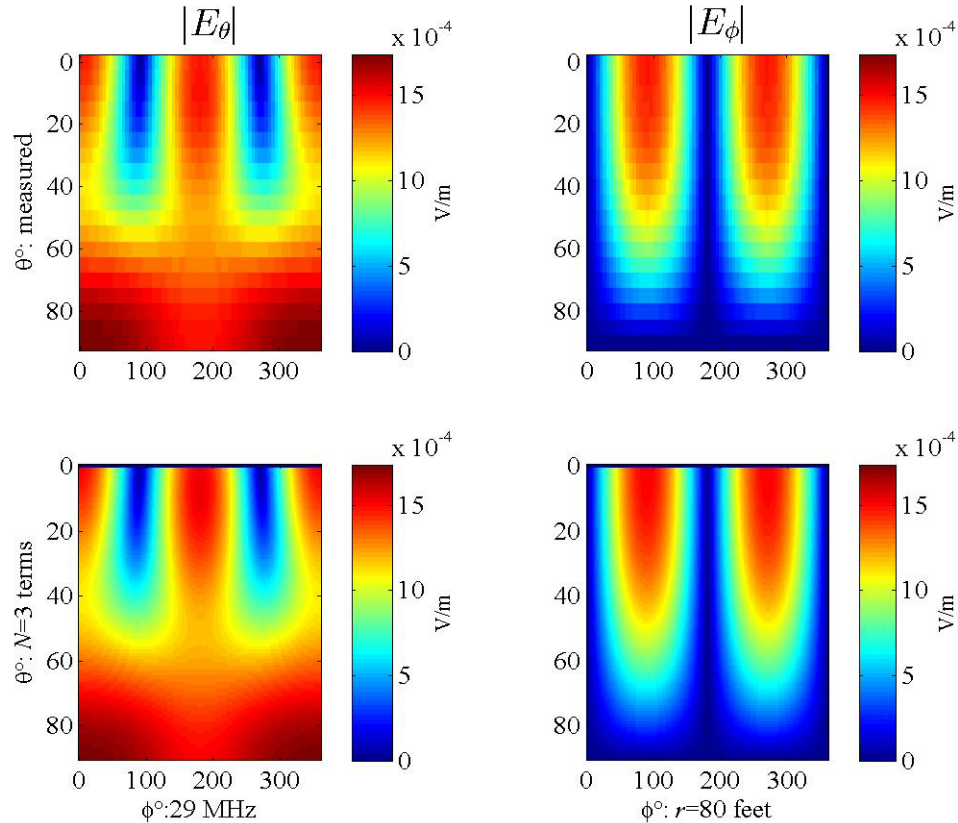
Figure 37: Tilted dipole synthesis at 29 MHz and the 80-ft radius. The upper panels are the sampled fields computed from MiniNEC. The lower panels are the synthesized fields.

9.2 Far Field

Figure 38 compares the far field computed by MiniNEC to Sarkar's expansion. The upper panels show the magnitude of the electric fields (V/m) computed by MiniNEC at the 500-ft radius. The sampling still uses the 5° increments. The lower panels show the magnitude of the electric fields computed by Sarkar's expansion. That is, the electric fields were sampled at an 80-ft radius, Sarkar's coefficients were estimated from these samples, and these coefficients compute the field at the 500-ft radius. The magnitude of these plots show good agreement.
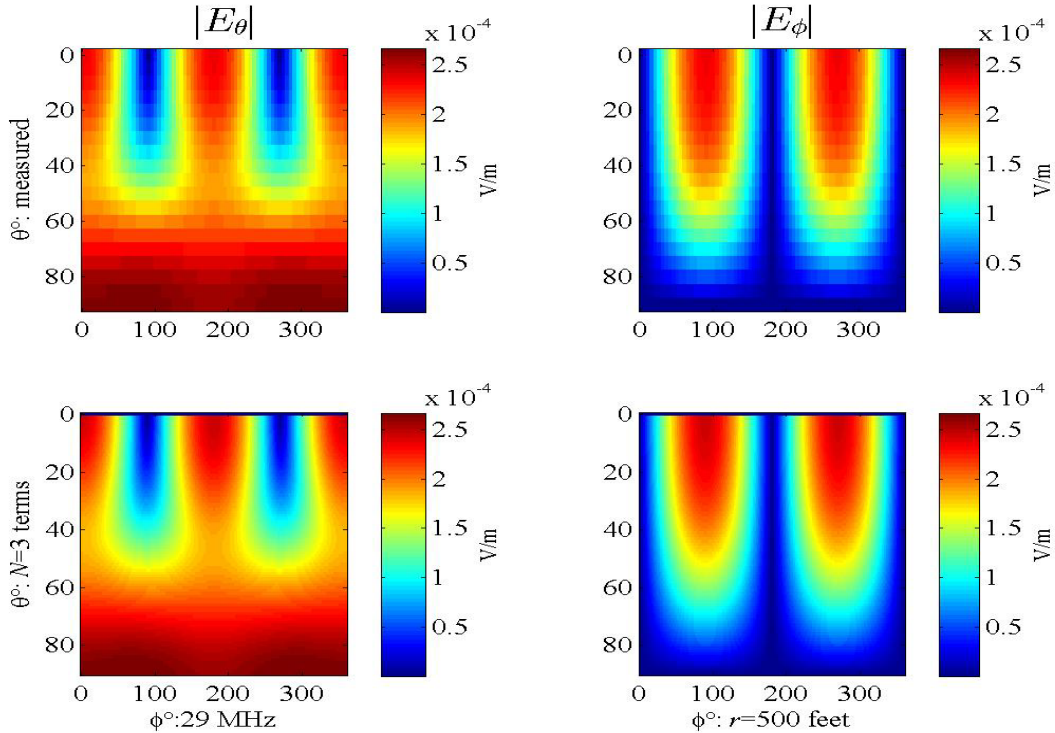
Figure 38: Comparing far-field patterns of the tilted dipole at 29 MHz. (upper panels) sampled fields computed from MiniNEC at the 500-ft radius. (lower panels) synthesized fields computed from the sampled fields at the 80-ft radius and extended to the 500-ft radius.

10 Shifted Tilted Dipole

Figure 33 is a schematic of the tilted dipole from the preceeding section that is shifted along the x-axis.
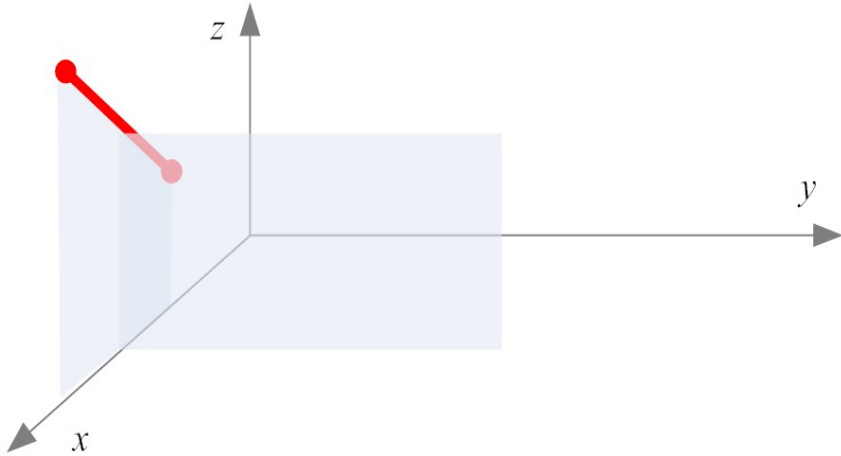
Figure 39: Dipole shifted along the x-axis, tilted in the $x \times z$-plane and lifted over a perfect ground.

This dipole is simulated in MiniNEC with the following specifications:

- Length $\ell = 8$ feet

- Tilted from vertical in the $x \times z$-plane by $\theta_T = 45°$

- Lifted over the ground by $h_G = 6$ ft

- Shifted along the x-axis by 10 ft

Table 24 lists the MiniNEC description for completeness, where the dipole is driven at 29 MHz. Figure 40 reports the resulting electric fields measured on a hemisphere with a radius of 80 ft or 24 m. At 29 MHz, the wavelength is approximately 10 m so that electric fields are measured on a hemisphere roughly 2.5 wavelengths from the antenna.

Table 24: MiniNEC description of the shifted, tilted dipole.

```
D:\antenna\NearToFarField\TiltedDipoleShifted\ShftedTiltedDipole_80  01-28-2013   14:50:23


Tilted Dipole
45 degrees elevation in the x-z plane
8 long
6 ft above the ground
Shifted 10 ft along the x-axis


GEOMETRY
Dimensions in feet
Environment: perfect ground

wire  caps X              Y              Z              radius         segs
 1    none 12.8284        0              8.8284         .001           12
          7.1716          0              3.1716


Number of wires        =   1
        current nodes  =  11


                          minimum                    maximum
Individual wires        wire    value            wire    value
segment length           1      .66666            1      .66666
segment/radius ratio     1      666.66            1      666.66
radius                   1      1.E-03            1      1.E-03


ELECTRICAL DESCRIPTION
Frequencies (MHz)
     frequency                   no. of  segment length (wavelengths)
 no. lowest       step          steps   minimum        maximum
 1   29.          0               1      .0196556       .0196556

Sources
source node     sector  magnitude      phase          type
 1      6         1      1.             0              voltage
```
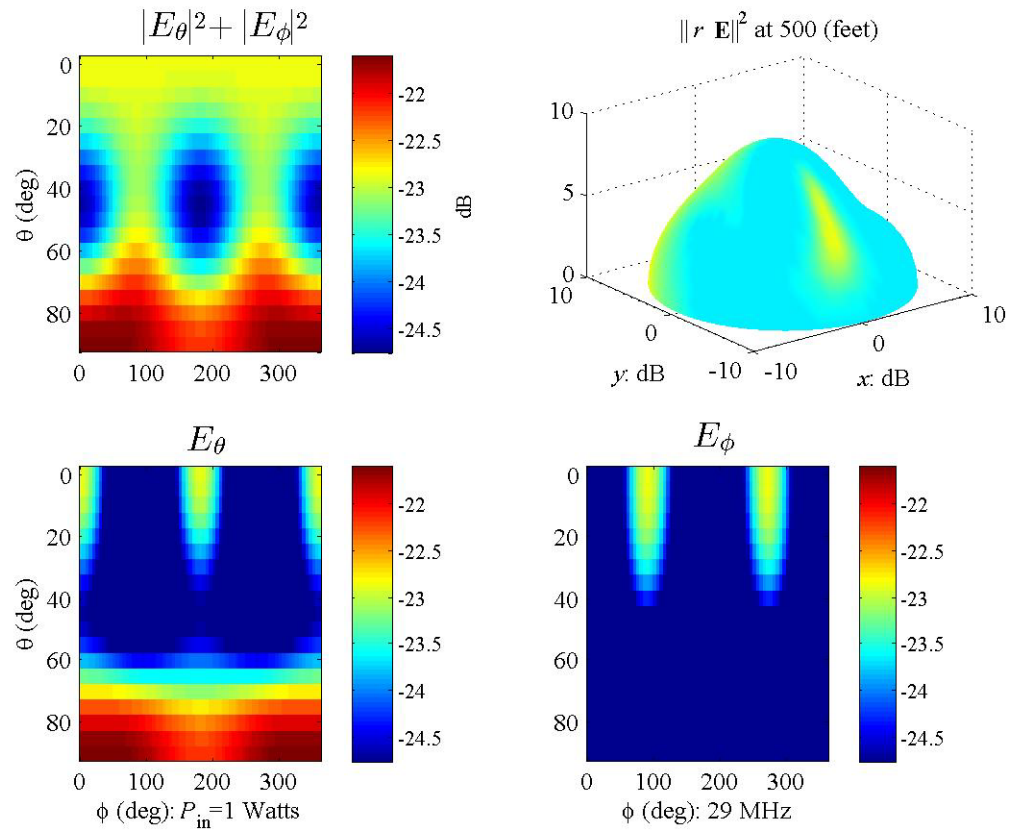
Figure 40: MiniNEC simulation of the shifted, tilted dipole at 29 MHz; electric fields are measured at 80 ft.

10.1   Synthesis

Synthesis requires extending the electric fields from the upper hemisphere to the entire sphere. If $E_\theta^+(\theta, \phi)$ and $E_\phi^+(\theta, \phi)$ denote the simulated electric fields on the upper hemisphere, make the even extension

$$E_\theta(\theta, \phi) = \begin{cases} E_\theta^+(\theta, \phi) & 0 \leq \theta \leq \pi/2 \\ E_\theta^+(\pi - \theta, \phi) & \pi/2 \leq \theta \leq \pi \end{cases}$$

and the odd extension

$$E_\phi(\theta, \phi) = \begin{cases} E_\phi^+(\theta, \phi) & 0 \leq \theta \leq \pi/2 \\ -E_\phi^+(\pi - \theta, \phi) & \pi/2 \leq \theta \leq \pi \end{cases} .$$

Tables 25, 26, 27, and 28 report the coefficients estimated from E_θ and E_ϕ sampled on the upper hemisphere. The hemisphere is sampled using 5° increments. There are $N_\phi = 73$ samples in $0 \leq \phi \leq 360°$ azimuth and $N_\theta = 19$ samples in $0 \leq \phi \leq 90°$ zenith. The 10-ft offset of the antenna required that the number of terms increase to $N = 5$ over $N = 3$ when there is no offset.

Table 25: $|\alpha_{mn}|$ estimated from E_θ and E_ϕ sampled on the sphere at 80 ft for the shifted, tilted dipole.

	$n = 1$	$n = 2$	$n = 3$	$n = 4$	$n = 5$
$m = 0$	$6.24 \cdot 10^0$	$8.17 \cdot 10^{-2}$	$1.69 \cdot 10^0$	$1.29 \cdot 10^{-1}$	$9.12 \cdot 10^{-2}$
$m = 1$	$5.76 \cdot 10^{-1}$	$4.12 \cdot 10^0$	$7.07 \cdot 10^{-2}$	$1.78 \cdot 10^{-1}$	$2.18 \cdot 10^{-2}$
$m = 2$		$6.61 \cdot 10^{-2}$	$3.98 \cdot 10^{-1}$	$1.16 \cdot 10^{-2}$	$7.96 \cdot 10^{-3}$
$m = 3$			$3.78 \cdot 10^{-3}$	$1.82 \cdot 10^{-2}$	$6.01 \cdot 10^{-4}$
$m = 4$				$1.23 \cdot 10^{-4}$	$4.93 \cdot 10^{-4}$
$m = 5$					$2.58 \cdot 10^{-6}$

Table 26: $|\beta_{mn}|$ estimated from E_θ and E_ϕ sampled on the sphere at 80 ft for the shifted, tilted dipole.

	$n = 1$	$n = 2$	$n = 3$	$n = 4$	$n = 5$
$m = 0$	0	0	0	0	0
$m = 1$	$2.79 \cdot 10^{-6}$	$2.48 \cdot 10^{-5}$	$1.80 \cdot 10^{-6}$	$6.84 \cdot 10^{-6}$	$1.20 \cdot 10^{-6}$
$m = 2$		$5.52 \cdot 10^{-6}$	$2.36 \cdot 10^{-6}$	$2.29 \cdot 10^{-7}$	$9.26 \cdot 10^{-7}$
$m = 3$			$3.75 \cdot 10^{-7}$	$8.52 \cdot 10^{-7}$	$5.98 \cdot 10^{-8}$
$m = 4$				$1.26 \cdot 10^{-8}$	$4.54 \cdot 10^{-8}$
$m = 5$					$2.31 \cdot 10^{-9}$

Table 27: $|\gamma_{mn}|$ estimated from E_θ and E_ϕ sampled on the sphere at 80 ft for the shifted, tilted dipole.

	$n = 1$	$n = 2$	$n = 3$	$n = 4$	$n = 5$
$m = 0$	$9.80 \cdot 10^{-9}$	$1.60 \cdot 10^{-7}$	$5.56 \cdot 10^{-8}$	$1.99 \cdot 10^{-7}$	$2.51 \cdot 10^{-7}$
$m = 1$	$2.34 \cdot 10^{-7}$	$9.91 \cdot 10^{-9}$	$2.24 \cdot 10^{-8}$	$7.46 \cdot 10^{-9}$	$2.49 \cdot 10^{-8}$
$m = 2$		$2.79 \cdot 10^{-8}$	$7.16 \cdot 10^{-9}$	$4.55 \cdot 10^{-9}$	$4.60 \cdot 10^{-10}$
$m = 3$			$5.78 \cdot 10^{-9}$	$2.53 \cdot 10^{-11}$	$3.43 \cdot 10^{-10}$
$m = 4$				$4.58 \cdot 10^{-10}$	$2.42 \cdot 10^{-11}$
$m = 5$					$9.58 \cdot 10^{-11}$

Table 28: $|\delta_{mn}|$ estimated from E_θ and E_ϕ sampled on the sphere at 80 ft for the shifted, tilted dipole.

	$n = 1$	$n = 2$	$n = 3$	$n = 4$	$n = 5$
$m = 0$	0	0	0	0	0
$m = 1$	$9.05 \cdot 10^{-3}$	$3.27 \cdot 10^{-4}$	$7.71 \cdot 10^{-6}$	$2.27 \cdot 10^{-5}$	$2.94 \cdot 10^{-5}$
$m = 2$		$1.07 \cdot 10^{-3}$	$2.89 \cdot 10^{-5}$	$1.08 \cdot 10^{-5}$	$1.37 \cdot 10^{-6}$
$m = 3$			$5.47 \cdot 10^{-5}$	$1.39 \cdot 10^{-6}$	$5.88 \cdot 10^{-7}$
$m = 4$				$1.57 \cdot 10^{-6}$	$3.89 \cdot 10^{-8}$
$m = 5$					$2.93 \cdot 10^{-8}$

10.2   Far Field

Figure 41 compares the MiniNEC fields to Sarkar's synthesized fields at a 500-ft ra-
dius. The upper panels are the sampled fields computed from MiniNEC. The lower
panels are the synthesized fields computed from Sarkar's expansion using the coeffi-
cients α_{mn}, β_{mn}, γ_{mn}, δ_{mn}, estimated from the sampled fields on the upper hemisphere
at the 80-ft radius. These images use the same linear color scale with the magnitude of
the fields plotted in V/m. Comparison between the sampled fields from MiniNEC and
the synthesized field of Sarkar shows that differences in the magnitudes are relatively
small.
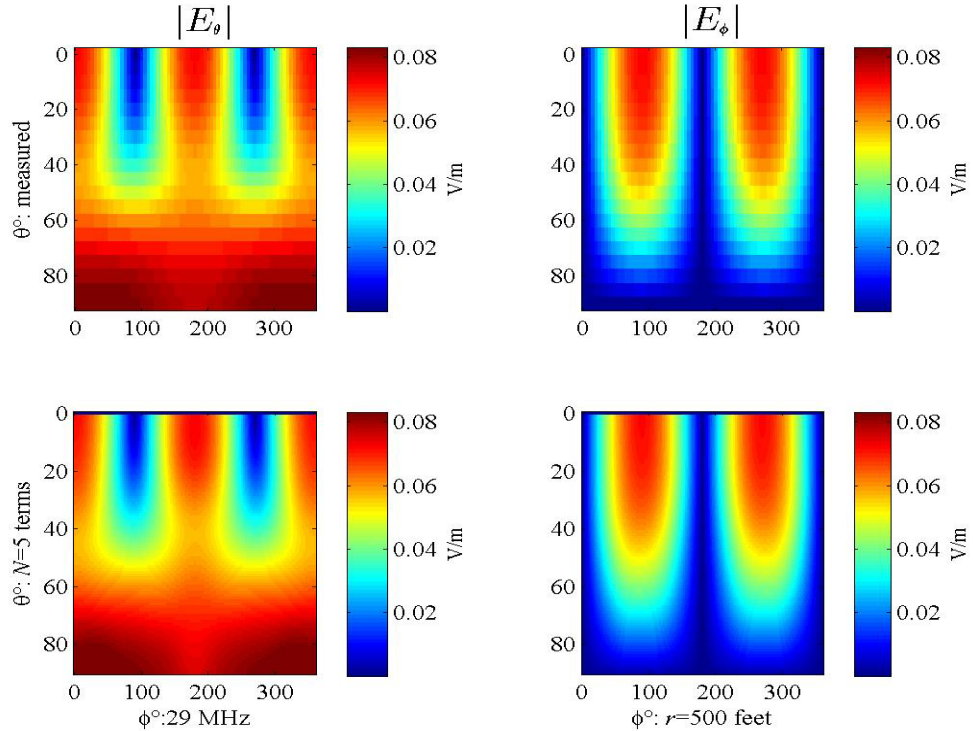
Figure 41: Comparing far-field patterns of the shifted, tilted dipole at 29 MHz. (upper
panels) sampled fields computed from MiniNEC at the 500-ft radius. (lower panels)
synthesized fields computed at the 80-ft radius and extended to the 500-ft radius.

11 "V" Dipole

Figure 42 is a schematic of a half-wavelength, "V" dipole lifted over the ground plane.
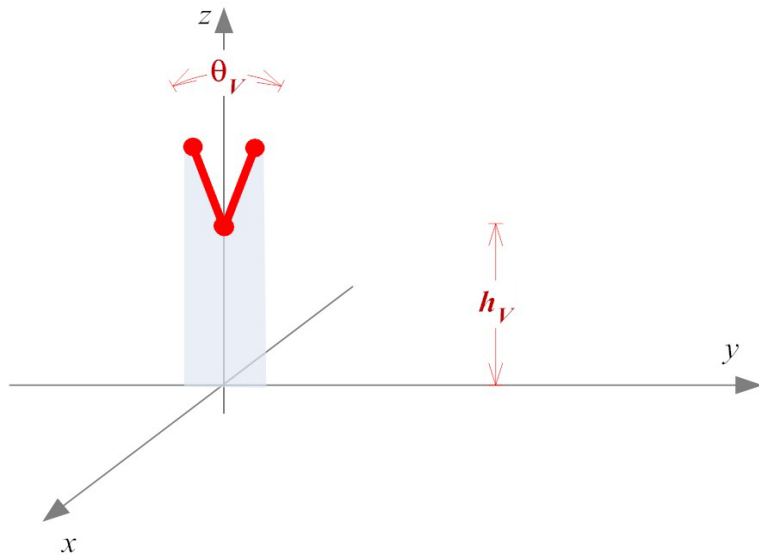
Figure 42: "V" dipole in the $y \times z$-plane and lifted over a perfect ground.

This dipole is simulated in MiniNEC at 300 MHz:

- Each leg of the "V" has length of $1/4$ m

- The angle between the legs is $\theta_V = 45°$

- The vertex is lifted over the ground by $h_G = 2$ m

Table 29 lists the MiniNEC description for completeness, where the dipole is driven at 300 MHz. Figure 43 reports the resulting electric fields measured on a hemisphere with a radius of 80 ft or 24 m. At 300 MHz, the wavelength is approximately 1 m so that electric fields are measured on a hemisphere roughly 24 wavelengths from the antenna.

Table 29: MiniNEC description of the "V" dipole.

```
D:\antenna\NearToFarField\vDipole\vDipole01_300MHz_80feet  02-06-2013   07:46:29


Vee dipole: 45 degrees
2 m above perfect ground

GEOMETRY
Dimensions in meters
Environment: perfect ground

wire  caps X                Y               Z               radius       segs
 1    none 0               -.0956709        2.23097         .0025         5
           0                0               2.
 2    none 0                0               2.              .0025         5
           0                .0956709        2.23097


Number of wires        =  2
        current nodes  =  9


                        minimum                 maximum
Individual wires     wire    value           wire   value
segment length       1       .05             1      .05
segment/radius ratio 1       20.             1      20.
radius               1       2.5E-03         1      2.5E-03


ELECTRICAL DESCRIPTION
Frequencies (MHz)
     frequency                no. of  segment length (wavelengths)
 no. lowest      step         steps   minimum       maximum
 1   299.8       0            1       .05           .05

Sources
source node    sector  magnitude      phase         type
 1      5        1      1.             0             voltage
```
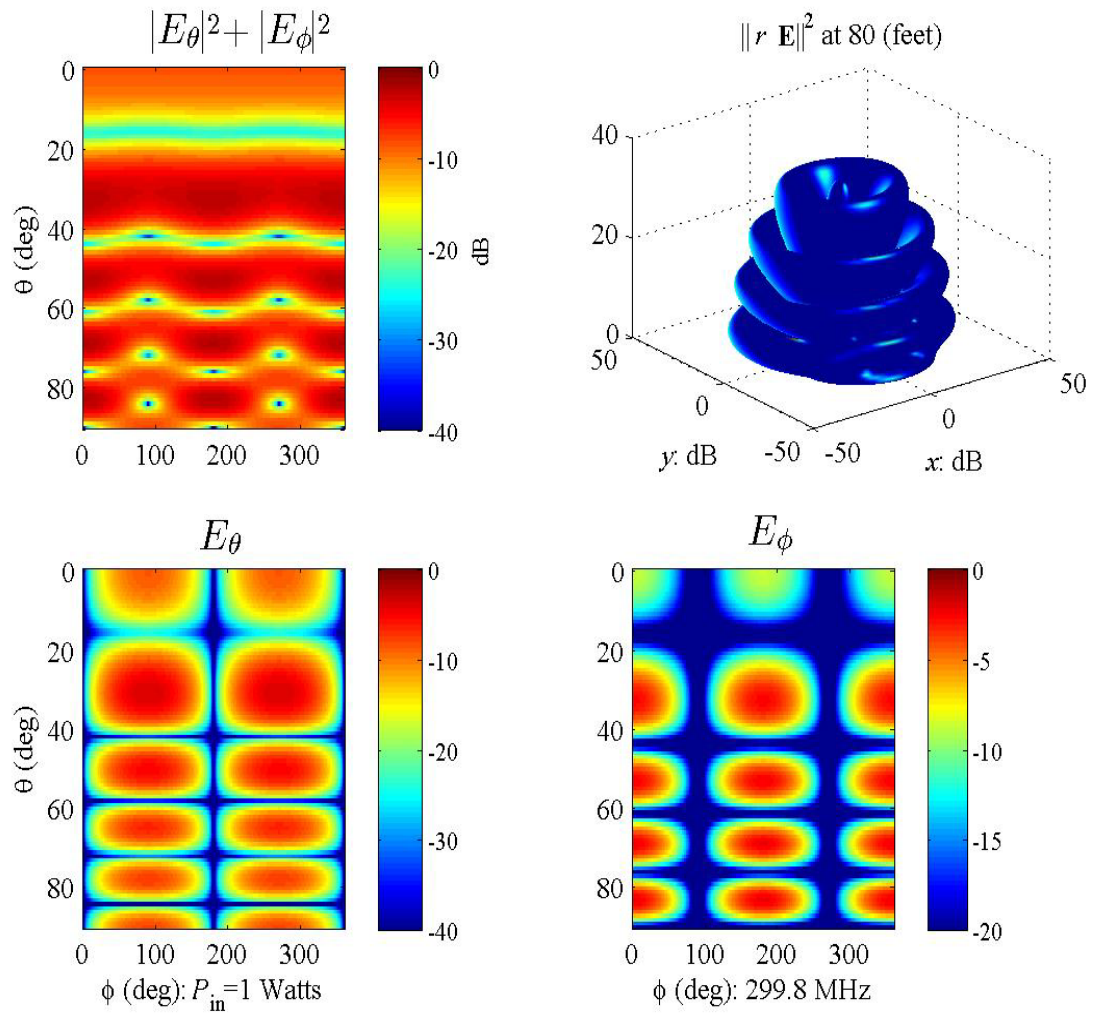
Figure 43: MiniNEC simulation of the "V" dipole at 300 MHz; electric fields are measured at 80 ft.

11.1   Synthesis

Synthesis requires extending the electric fields from the upper hemisphere to the entire sphere. If $E_\theta^+(\theta, \phi)$ and $E_\phi^+(\theta, \phi)$ denote the simulated electric fields on the upper hemisphere, make the even extension

$$E_\theta(\theta, \phi) = \begin{cases} E_\theta^+(\theta, \phi) & 0 \leq \theta \leq \pi/2 \\ E_\theta^+(\pi - \theta, \phi) & \pi/2 \leq \theta \leq \pi \end{cases}$$

and the odd extension

$$E_\phi(\theta, \phi) = \begin{cases} E_\phi^+(\theta, \phi) & 0 \leq \theta \leq \pi/2 \\ -E_\phi^+(\pi - \theta, \phi) & \pi/2 \leq \theta \leq \pi \end{cases} .$$

Figure 44 reports Sarkar's coefficients estimated from E_θ and E_ϕ sampled on upper hemisphere of an 80-ft sphere. This hemisphere is sampled using $5°$ increments. There are $N_\phi = 73$ samples in azimuth ($0 \leq \phi \leq 360°$) and $N_\theta = 19$ samples in zenith ($0 \leq \phi \leq 90°$).
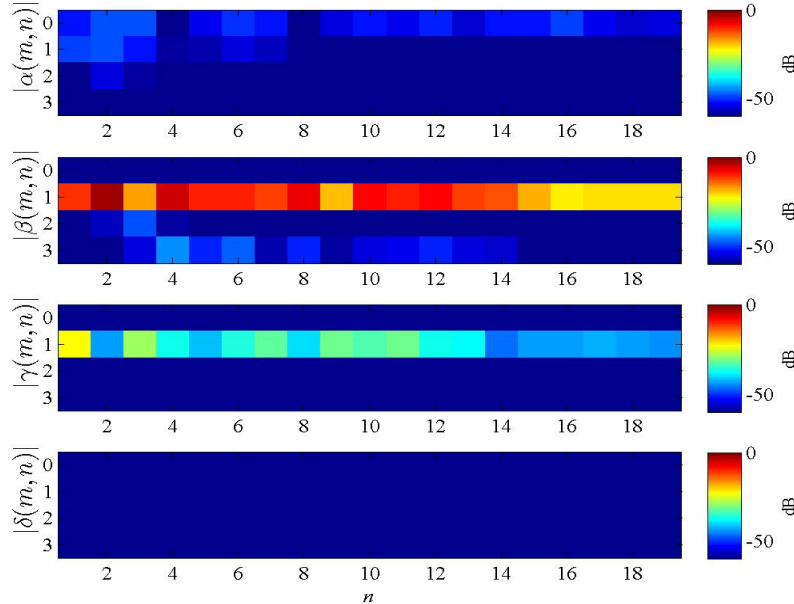
Figure 44: Sarkar's coefficients estimated from E_θ and E_ϕ sampled on the sphere at 80 ft for the "V" dipole.

The coefficients are plotted in dB (i.e., $10 \times \log_{10}(|\alpha(m, n)|)$) so that each decade corresponds to a power of 10. The plot shows contributions from β and γ. The slow "roll-off" of β implies that convergence will be slow.

For example, Figure 45 reports on using $N = 11$ coefficients to synthesize the electric fields at 80 ft. The upper panels are the electric fields computed from Mini-NEC at a radius of 80 ft and are the "ground truth." The lower panels are the synthesized electric fields at 80 ft. The synthesis starts by sampling both fields on the 80-ft upper hemisphere at 5° increments, extending both fields to the whole 80-ft sphere, estimating Sarkar's coefficients from the samples, and finally, using the estimated coefficients to synthesize the field at $r = 80$ ft. The lower panels show that the gross structure of the fields are approximated while the magnitudes needs more terms to "fill-in."
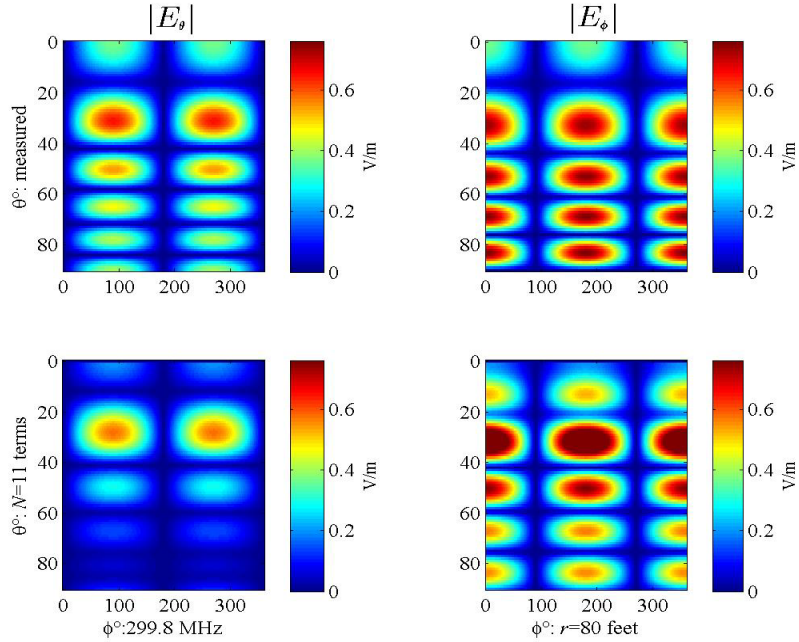

Figure 45: Near-field synthesis using $N = 11$, $M = 3$.

Figures 46 and 47 show that increasing the number of terms produces synthetic fields with increasing accuracy. The final plot is considered "good enough" to extend to the far field.

71
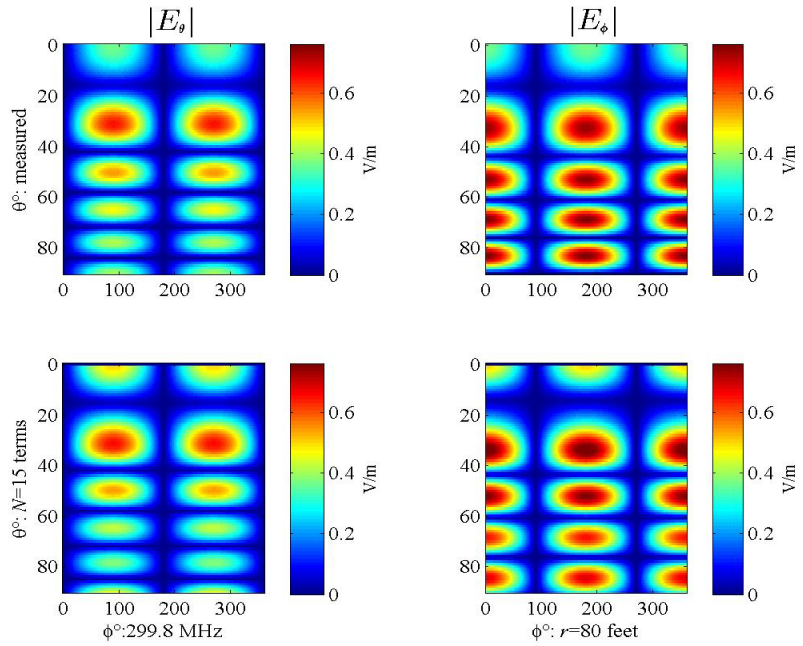
Figure 46: Near-field synthesis using $N = 15$, $M = 3$.
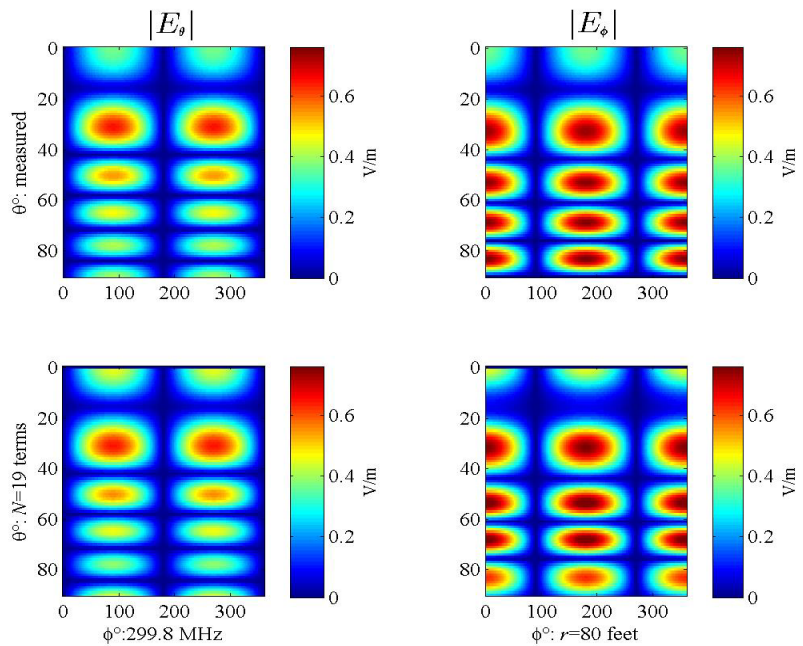
Figure 47: Near-field synthesis using $N = 19$, $M = 3$.

11.2 Far Field

Figure 48 reports on the far-field synthesis at 500 ft. The upper panels are the electric fields computed from Mini-NEC at 500 ft. The lower panels are the corresponding synthetic field at 500 ft. These synthetic fields were produced by sampling the Mini-NEC fields at $r = 80$ ft on upper hemisphere at $5°$ increments, extending both fields to the whole 80-ft sphere, estimating Sarkar's coefficients from these samples, and finally, using these estimated coefficients to synthesize the field at $r = 500$ ft. The lower panels show that the $N = 19$ terms produces an approximation that can support a gain computations.
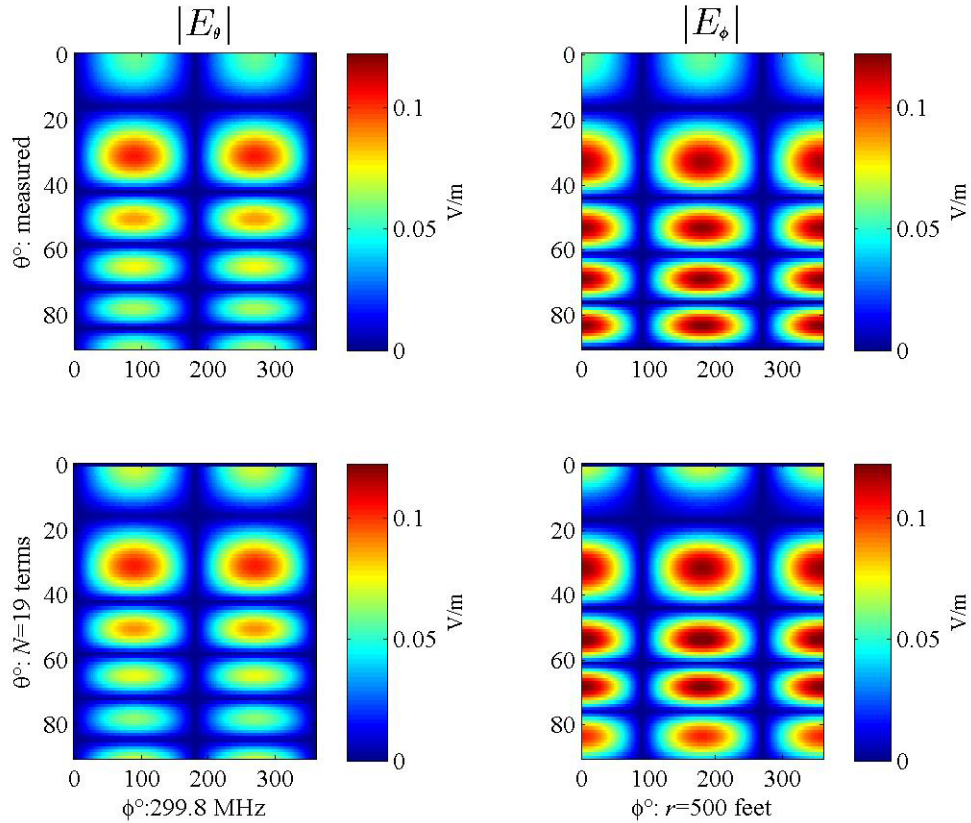

Figure 48: "V" dipole synthesis at $r = 500$ ft from E_θ and E_ϕ sampled on the upper hemisphere at 80 ft.

73

11.3   Far-Field Gains

The radiation intensity is defined for the far field as [4, Equation 2-12a]

$$U(\theta, \phi) := \frac{r^2}{2\eta} \left\{ |E_\theta(\theta, \phi)|^2 + |E_\phi(\theta, \phi)|^2 \right\} \quad \text{[Watts]}.$$

Figure 49 compares the radiation intensity for the "V" dipole between the Mini-NEC "ground truth" (upper panel) and the a synthetic approximation constructed from $N = 19$ terms (lower panel). The range for both fields is 500 ft. At 300 MHz, this corresponds to 152 wavelengths. The synthetic radiation intensity exhibits discrepancies for increasing zenith or decreasing elevation angle. For zenith of 0°, the synthesis algorithms used in this report set the field to zero
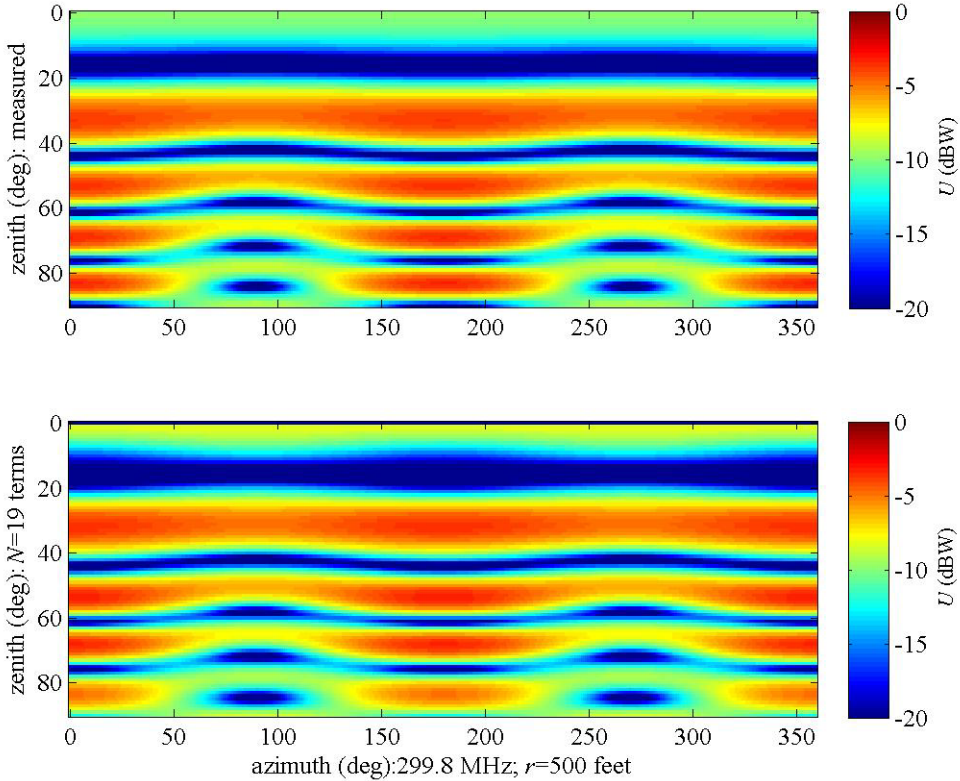

Figure 49: "V" dipole radiation intensity at $r = 500$ ft from E_θ and E_ϕ sampled on the upper hemisphere at 80 ft.

12 Phase 2 Tasking

Phase 1 assessed an implementation of Sarkar's near-to-far transformation [12] on analytic antenna models and Mini-NEC antenna simulations. For both classes of antenna models, Phase 1 verified the implementation recovers the far field from the near field—provided the spherical expansion includes a sufficient number of terms. That is, the truncation error governs the near-to-far transform rather than the discretization error—assuming noise-free antenna models (see the discussion for Equation 2).

Phase 2 applies Sarkar's near-to-far transformation to measurements taken at SSC Pacific's Antenna Pattern Range. These electric field measurements are degraded by additive noise, in-band RF interference, and the mechanical and electrical variations in the Antenna Pattern Range. Therefore, an initial task for Phase 2 is to assess the robustness of the near-to-far transformation with respect to the noise-corrupted measurements. Figure 50 shows the candidate reference antenna placed on the Antenna Pattern Range. This antenna consists of a monopole and a loop above the ground plane.

Figure 50: Reference antenna in the SSC Pacific Antenna Pattern Range.

Because this antenna is amenable to modeling, comparison of the ideal model against the measured antenna is possible and will produce a noise model for the spherical coefficients. Although the near-to-far transformation is not expected to amplify the noise in the far field, the accuracy of the spherical coefficients may degrade the asymptotic estimates of the truncation error. The noise model can set a truncation limit—increasing the number terms in the expansion may not improve the accuracy because the higher-order coefficients are lost in the noise.

Classical statistical smoothing is a standard approach to reduce additive noise but will not mitigate system measurement errors. Assessing the payoff for this smoothing is a necessary Phase 2 task. A more promising approach uses model identification to mitigate noise. In this approach, an antenna model is fitted to the noisy measured near field. For example, measurements of the candidate monopole may be fitted by varying antenna length, radius, orientation, and material. Once a model is determined that best "explains" the measurements, this model is then used to compute a "noise-free" far field and extrapolate to other frequencies.

References

[1] Abramowitz, Milton and Irene A. Stegun [1972] *Handbook of Mathematical Functions*, Dover Publications, Inc., New York, NY.

[2] Andrews, Larry C. [1985] *Special Functions for Engineers and Applied Mathematicians*, Macmillan Publishing Company, New York, NY.

[3] Arfken [1970] *Mathematical Methods for Physicists*, Academic Press, Inc., New York, NY.

[4] Balainis, Constantine A. [1997] *Antenna Theory*, second edition, John Wiley & Sons, Inc., New York, NY.

[5] Corson, Dale R. and Paul Lorrain [1962] *Introduction to Electromagnetic Waves*, W. H. Freeman and Company, San Francisco, CA.

[6] Rockway J., J. Meloling, J. C. Allen [2011] *Interpolating Spherical Harmonics for Computing Antenna Patterns*, SPAWAR Technical Report 1999.

[7] Edminister, Joseph A. [1993] *Electromagnetics, second edition*, Schaum's Outline Series, McGraw-Hill, New York, NY.

[8] Francis, Michael H. ; Ronald C. Wittmann; Jin-Seob Kang [2005] Uncertainties in Spherical Near-Field Antenna Measurements, *Proceedings of ISAP2005*, Seoul, Korea.

[9] `http://hiqantennas.com`.

[10] Jackson, J. D. [1975] *Classical Electrodynamics*, 2nd edition, Wiley.

[11] Marie, F.; L. Bertel; Y. Erhel; D. Lemur; M. Oger [2005] Beam Forming Techniques Operating on HF Collocated Antennas.

[12] Sarkar, T.K., P. Petre, A. Taaghol, R.F. Harrington [1997] An Alternative Spherical Near Field to Far Field Transformation, *Progress in Electromagnetics Research, PIER* 16, pages 269–284.

[13] Stoer, J. and R. Bulirsch [1980] *Introduction to Numerical Analysis*, Springer-Verlag, New York, NY.

1. REPORT DATE (DD-MM-YYYY) September 2014	2. REPORT TYPE Final	3. DATES COVERED (From - To)

4. TITLE AND SUBTITLE A Near-to-Far Transformation using Spherical Expansions Phase 1: Verification on Simulated Antennas	5a. CONTRACT NUMBER
	5b. GRANT NUMBER
	5c. PROGRAM ELEMENT NUMBER
6. AUTHORS J. H. Meloling J.C. Allen	5d. PROJECT NUMBER
	5e. TASK NUMBER
	5f. WORK UNIT NUMBER

7. PERFORMING ORGANIZATION NAME(S) AND ADDRESS(ES) SSC Pacific, 53560 Hull Street, San Diego, CA 92152–5001	8. PERFORMING ORGANIZATION REPORT NUMBER TR 2058

9. SPONSORING/MONITORING AGENCY NAME(S) AND ADDRESS(ES) Office of the Director of National Intelligence Intelligence Advanced Research Projects Activity Washington, DC 20511	10. SPONSOR/MONITOR'S ACRONYM(S)
	11. SPONSOR/MONITOR'S REPORT NUMBER(S)

12. DISTRIBUTION/AVAILABILITY STATEMENT
Approved for public release.

13. SUPPLEMENTARY NOTES
This is work of the United States Government and therefore is not copyrighted. This work may be copied and disseminated without restriction.

14. ABSTRACT

Tapan Sarkar wrote a substantial technical paper on a transformation mapping an antenna's near-field into its far field. A numerical implementation of Sarkar's "near-to-far" transformation is assessed in this report. This report assesses this "near-to-far" implementation on the following antenna models using only a finite number of near-field samples:

• Analytic antenna models where the near field, far field, and the spherical expansions are computable in closed form,
• Mini-NEC antenna simulations where the near field, far fields and spherical expansions are numerically computed.

The implementation described in this report demonstrates that an antenna's far field can be extracted from sampled near field measurements—provided the spherical expansion includes a sufficient number of terms and that the near-field samples are sufficiently dense. Phase II of this effort extends the implementation to estimate the number of spherical coefficients necessary to deliver user-specified accuracy in the far field and how noisy the near-field measurements affect the far field approximation.

15. SUBJECT TERMS
Mission Area: Communications
near-to-far field transformations   Sarkar's near-to-far transformations   Hertzian electric dipole   small loop antenna
horizontal electric dipole   tilted dipole   shifted tilted dipole   "V" dipole

16. SECURITY CLASSIFICATION OF:			17. LIMITATION OF ABSTRACT	18. NUMBER OF PAGES	19a. NAME OF RESPONSIBLE PERSON J. H. Meloling
a. REPORT	b. ABSTRACT	c. THIS PAGE			19B. TELEPHONE NUMBER (Include area code)
U	U	U	U	80	(619) 553-2134

Standard Form 298 (Rev. 8/98)
Prescribed by ANSI Std. Z39.18

INITIAL DISTRIBUTION

Approved for public release.

SSC Pacific
San Diego, CA 92152-5001